WILEY | Hindawi

Research Article

Mineralized Granitic Porphyry of the Yangla Copper Deposit, Western Yunnan, China: Geochemistry of Fluid Inclusions and H-O, S, and Pb Isotopes

Xinfu Wang,[1] Bo Li [ID],[1] ShenJin Guan,[1] Olivier Nadeau,[2] and Guo Tang[1]

[1]*Faculty of Land and Resource Engineering, Kunming University of Science and Technology, Wuhua, Kunming 650093, China*
[2]*Department of Earth and Environmental Sciences, University of Ottawa, Ottawa, Ontario, Canada*

Correspondence should be addressed to Bo Li; libo8105@qq.com

The Yangla copper deposit (YCD) is located in the central part of the Jinshajiang tectonic belt (Jinshajiang metallogenic belt) and is one of the most important copper deposits which has the large-scale copper reserves of the northwestern Yunnan, China. The ore bodies are strictly controlled by the stratum, pluton, and structure, which are layered, lens, and vein-like within the contact or fracture zone of the pluton and surrounding rock. At Yangla, two styles of mineralization occur at the brecciated contact zone between the pluton (granodiorite and granitic porphyry) and carbonaceous wall rock and include strata bound/lens-shaped replacement of carbonate rocks (skarn style) and porphyry-style sulfide-quart-calcite veins. But, the granitic porphyry mineralization have received less attention; the isotope and fluid inclusion studies are relatively scarce for limited porphyry ore bodies that have been discovered at the YCD. Quartz-hosted fluid inclusions from the recently discovered granitic porphyry have homogenization temperature averaging around $180 \pm 20°C$ and $300 \pm 20°C$ with salinities ranging from 4 to 22 wt.% $NaCl_{eq}$, pointing toward the contribution of medium temperature-medium salinity and low temperature-low salinity fluids during the metallogenesis. These fluid inclusions have $\delta^{18}O_{H2O}$ values ranging between -1.91‰ and -1.02‰ and δD values ranging between -143.10‰ and -110‰, suggesting that the ore-forming fluid was a mix of magmatic and meteoric water. Ore-related pyrite/chalcopyrite have $\delta^{34}S_{V-CDT}$ values ranging from -1.0‰ to 1.0‰ and whole rocks have $\delta^{34}S_{\Sigma S} = 0.34$, suggesting that sulfur mainly derived from magmatic rocks of the Yangla mining area. The sulfides $^{208}Pb/^{204}Pb$ ranged from 38.8208-38.9969, $^{207}Pb/^{204}Pb$ from 15.7079-15.7357, and $^{206}Pb/^{204}Pb$ from 18.5363-18.7045, indicating that the lead mainly originated from the upper crust. It is demonstrated that the evolution of ore-forming fluid is continuous from the skarn ore body (SOB) stage to the porphyritic ore body stage and belong to the products of the same ore-forming fluid system, and the unisothermal mixing and cooling actions were maybe the main mechanism at the metallic minerals precipitation in mineralized granitic porphyry (MGP). A model is proposed according to the early stage, a magmatic fluid reacted and replaced with the surrounding carbonate rocks and then formed skarn-type ore bodies. The magmatic-hydrothermal fluid subsequently deposited porphyry-type quartz-calcite veins, veinlets, and stockwork mineralization.

1. Introduction

The YCD is located in the Yangla Township, Deqin County, Yunnan Province of southwestern China. Its tectonic location is in the central part of the Jinshajiang belt, between the Zhongzan-Zhongdian and the Changdu-Simao block. It is one of the most important copper deposits in the "Sanjiang" region (Jinshajiang, Lancangjian, and Nujiang),

with an average copper grade of ~1% and prospective reserves of 1.2×10^6 t of ore [1]. In recent years, extensive research has been undertaken on the YCD with the goal of documenting their geologic characteristics [1–5], structural feature [5–12], tectonogeochemical features [13, 14], isotopic ages of plutons and skarn ore bodies [9–12, 15–23], genesis of ores [2, 8, 17–19, 24], and fluid inclusions [17, 24–29]. In contrast, porphyry mineralization has received less attention;

systematic isotope and fluid inclusion studies are relatively scarce for limited porphyry-type copper deposit that have been discovered from the Yangla region.

As an important Cu producer in SW China, crystallization and ore-forming ages of the Yangla ore district attracted much attention, and the timing of granodiorite pluton and skarn ore bodies have been constrained to the Triassic (208-239 Ma, average 230 Ma) and Triassic (228-235 Ma, average 230 Ma) by the precise zircon U-Pb, biotite and hornblende Rb-Sr, and molybdenite Re-Os dating, respectively [9–12, 15–20, 22, 23]. These results have revealed the fact that skarn ore bodies was basically contemporary with granodiorite pluton in the YCD. Besides, for the YCD, the H-O isotopic composition of quartz was interpreted to be derived from the mixing of magmatic and meteoric water in skarn ore bodies [9–12, 24, 25, 27, 28, 30]. The sulfur isotopic signature of ore-related sulfides was interpreted to originate from the magmatic rocks (granodiorite pluton) of the Yangla region [9–12, 19, 24, 25, 27, 31] and that of lead is believed to have resulted from the mixing of mantle crustal materials in skarn ore bodies [9–12, 17, 19, 25–27, 29, 32–34]. So far, however, no systematic studies of the porphyry plutons of YCD and only preliminary studies have been conducted on the geochemical characteristics of the granitic porphyry dike [35]. So, the genetic relationships between porphyry plutons and Cu mineralization, origin and evolution of the deposit, and the metallogenic processes involved remain unclear. In recent years, a granitic porphyry dike closely associated with Cu mineralization was discovered at the tunnel 3250 m level in the process of geological prospecting in Yunnan Copper Industry (Group) Co. Ltd., 2014, which are suggesting the potential contribution of porphyry plutons to the Cu deposits at depth.

In this study, we present a study of fluid inclusions and stable (H-O-S) and radiogenic (Pb) isotope systematics of the MGP, YCD. The fluid inclusion results combined with isotopic data provide clear constraints in particular to explain the origin, evolution, and mechanisms of the ore-forming fluids. We hope that this study can provide a scientific basis for further mineral prospecting and future prospecting of new Cu deposits in this area.

2. Geological Context

2.1. Geologic Setting. The "Sanjiang" metallogenic belt (Sanjiang: Jinshajiang, Langcanjiang, and Nujiang) is located at the southwest edge of Yangtze craton, southwest China (Figure 1(a)). The large-scale Yangla copper ore region is located in the paleo-Tethyan orogenic belt of the central Sanjiang region (Figure 1(b)), clamped between the regional Jinshajiang and Yangla faults, which have an approximately N-S orientation (Figure 1(c)). In this region, the base of the Yangtze continental plate has experienced multiple geologic transformations due to extension, rift sag, subduction, and collision, which have resulted in the formation of multiple arc-basins [28, 32]. The Jinshajiang paleo-Tethyan tectonic belt began rifting during the late Devonian, expanding into the Carboniferous-Permian basin (360-252 Ma). During the late stages of the early Permian, the Jinshajiang ocean basin

was subducted to the west beneath the Changdu-Simao block (252-200 Ma). Because of an E-W trend compression/-squeezing action, a series of low-angle thrust faults oriented toward the northwest was formed in the Jinshajiang belt [9–12]. At the same time, the subduction of the Jinshajiang ocean basin resulted in partial melting of the lower crust, forming large amounts of intermediate-to-evolved magma, large-scale volcanic and magmatic activity [9–12, 19, 24, 28], and granodioritic magmatism at 208-239 Ma, average 230 Ma [9–12, 16, 19, 32, 34]. Continued subduction also metasomatized and fertilized the mantle wedge and may also have led to the accumulation of a free volatile phase in the mantle wedge [9–12, 16, 32]. During the early Late Triassic (252-228 Ma), the tectonic environment transitioned from compressive to extensional tectonics, allowing the continuous upward migration of magmatic fluid and promotion of ore migration [32, 34]. It is believed that when the magmatic fluid within the mantle wedge reached the bottom of the early granodiorite pluton, the board-shaped or plate-shaped granodiorite pluton obstructed the upward migration and emplacement of the late-stage magmatic fluid [24, 32, 34]. The magmatic fluid was enriched in ore elements either in the reverse fault system of this early pluton or after migrating along rock fissures by infiltrating and metasomatizing carbonate rocks [9–12, 16]. The YCD thus appears to have formed during the early Late Triassic (252-228 Ma). Moreover, the tectonic background of the Jinshajiang tectonic belt involved large-scale magmatic fluid activity caused by the transition from compressive to extensional tectonics [9–12, 16, 19, 25, 27].

2.2. Ore Geology. The YCD is composed of 7 main ore blocks: Beiwu, Nilv, Linong, Jiangbian, Lunong, Tongjige, and Jiaren (Figure 1(c)). The surface geology of the region consists mainly of Silurian quartzite, marble with schist, Devonian marble, quartzite, sericite sandy slate, and Carboniferous basalt. The ore-bearing strata are mainly composed of the Devonian Jiangbian Formation (D_1j) and the Linong Formation ($D_{2+3}l$), while the ore-bearing lithology is dominated by diopside garnet skarns, followed by marble, quartzite, sericite sandy slate, granodiorite, and granitic porphyry.

The mining camp is characterized by a strong strctural control. In addition to the Jinshajiang and the Yangla faults, F4 faults run in the NE direction and a large number of interlayer fracture zones and secondary structural fractures have also developed [6, 32]. Regional faults control the spatial distribution of plutons and ore bodies, while NE-trending faults cause the plutons and ore bodies to fracture, forming various ore blocks and plutons. The contacts between the magmatic intrusions and the surrounding wall rock control the morphology of skarn ore bodies that are close to the contact zone. Interlayer faults control the morphology of stratiform ore bodies, fissures within plutons control the morphology of vein-type ore bodies, and fissures at the top and the boundaries of plutons are usually filled with quartz-sulfide veinlets. The late-stage NE-trending faults control the morphology of late-stage hydrothermal vein deposits [6].

Magmatic rocks are widely distributed within the mining camp. Extrusive rocks, intrusive rocks, and dyke rocks all
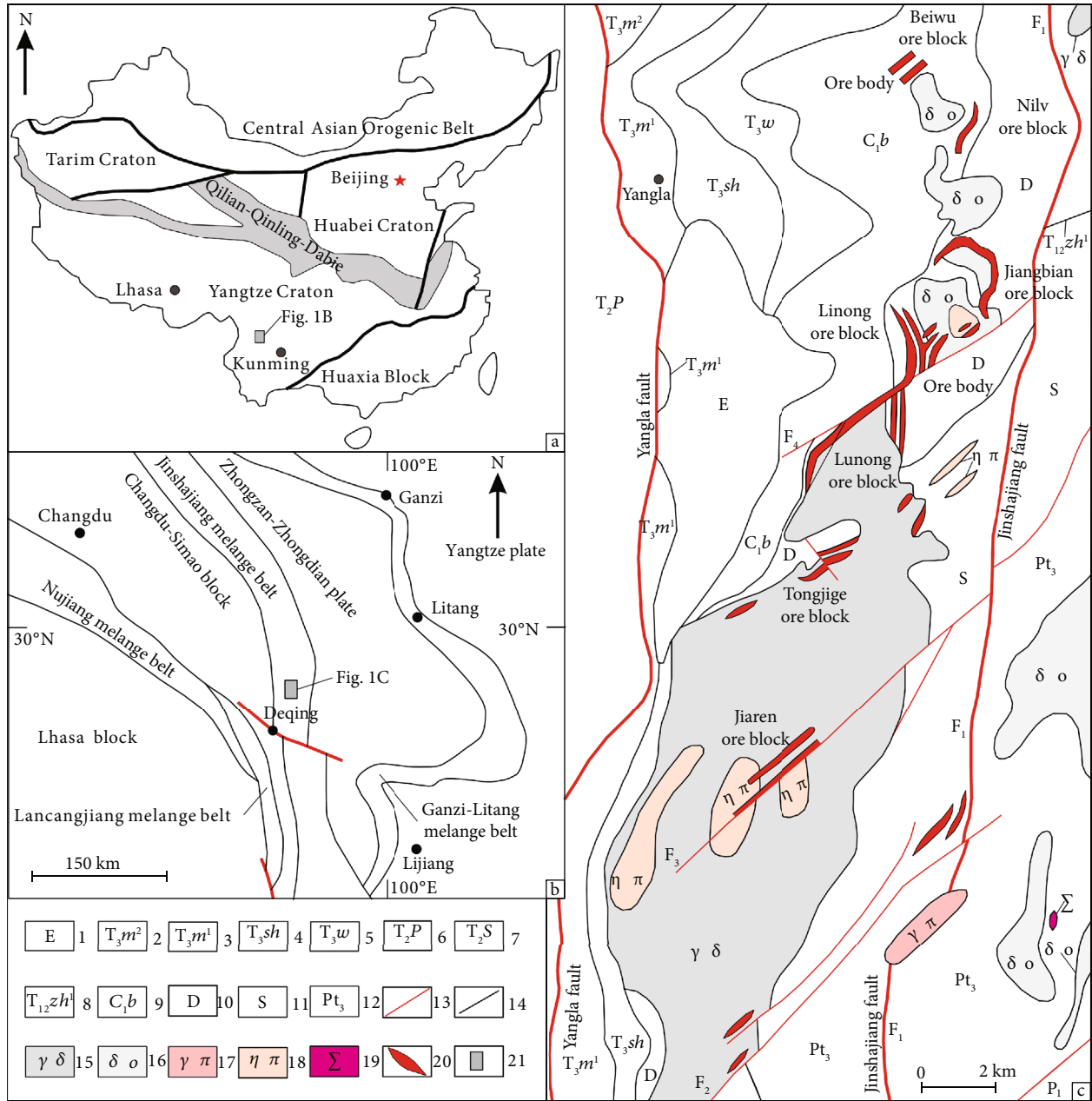
FIGURE 1: (a) The location of the Yangtze craton, the study area, in southwest China (modified after Zhu et al. [34]). (b) A regional geological map of the the study area, southwest China (modified after [9–12]). (c) A geological sketch map of the YCD, Yunnan, China (modified after [6]). 1-Paleogene, 2-Triassic (Maichuqing formation), 3-Triassic (Maichuqing formation), 4-Triassic (Sanhedong formation), 5-Triassic (Waigushucun formation), 6-Triassic (Pantiange formation), 7-Triassic (Zhongxinrong group), 8-Triassic(Shanglan formation), 9-lower Carboniferous (Beiwu formation), 10-Devonian, 11-Silurian, 12-Neoproterozoic, 13-fault, 14-geological boundary, 15-Granodiorite, 16-Quartz-diorite, 17-Granitic porphyry, 18-Monzonite granite, 19-Hercynian (ultrabasic rock), 20-Copper ore bodies, 21-the study area.

have developed. Extrusive rocks mainly consist of andesites and basalts (362 Ma and 296 Ma) (Table 1, Figure 2) and appear to have little association with ore formation [21]. Intrusive rocks were mainly formed during the Indosinian Period (208-239 Ma, and it is concentrated between 227 and 238 Ma, with an average 230 Ma) (Table 1, Figure 2) are mainly granodiorites and are spatially related to the ore deposits. From north to south, the intrusive rocks can be divided into the Beiwu, Linong, Lunong, and Jiaren plutons.

Moreover, each granodiorite pluton intrudes into the overlying Devonian marble, quartzite, and sericite sandy slate. All plutons may also have had the same magma source [4, 15, 16, 34]. Four plutons along the west side of Jinshajiang assume a linear distribution, forming the NNE-oriented granitic belt [34]. Among these, the Linong ore block, which is located in the central part, is the most fertile pluton in this mining area. It extends 2 km along the S-N direction and 1.5 km along the E-W direction, is exposed over about

TABLE 1: The statistical data of the diagenetic and metallogenic ages in Yangla copper deposit, Yunnan China.

Objects		Methods	Category	Age/Ma	References
Basalt	Zircon	U-Pb	Diagenetic	362.0 ± 8.0, 296.1 ± 7.0	[21]
Granodiorite	Biotite	Rb-Sr	Diagenetic	227	[20]
	Hornblende			208	
Masanophyre	Whole rock	Rb-Sr	Diagenetic	202	[35]
Granodiorite	Zircon	U-Pb	Diagenetic	229.6 ± 4.4	[22]
Granodiorite	Zircon	U-Pb	Diagenetic	238.1 ± 5.30, 239.0 ± 5.7, 227.9 ± 5.1, 213.6 ± 6.9	[15]
Diabase				222.0 ± 1.0	
Granodiorite	Zircon	U-Pb	Diagenetic	233.0 ± 1.4, 231.0 ± 1.6, 233.9 ± 1.4	[19]
Granodiorite	Zircon	U-Pb	Diagenetic	234.1 ± 1.2, 235.6 ± 1.2	[16]
Granodiorite	Zircon	U-Pb	Diagenetic	230.0 ± 1.9, 234.0 ± 0.8, 232.0 ± 0.5, 232.0 ± 0.9, 232.9 ± 0.9, 238.0 ± 0.5, 223.0 ± 0.9, 224.0 ± 0.7, 232.0 ± 1.1, 234.0 ± 1.2	[18]
SOB	Molybdenite	Re-Os	Metallogenic	230.9 ± 3.2	[16]
SOB	Molybdenite	Re-Os	Metallogenic	230.9 ± 3.3, 232.1 ± 3.3, 230.9 ± 3.3, 232.9 ± 3.3, 232.7 ± 3.5, 231.7 ± 3.3	[19]
SOB	Molybdenite	Re-Os	Metallogenic	230.9 ± 3.2, 233.0 ± 3.4, 229.7 ± 3.3, 229.7 ± 3.3, 230.6 ± 3.4, 233.3 ± 3.8, 233.6 ± 3.5, 234.2 ± 3.6, 230.7 ± 3.2, 234.8 ± 3.4	[9–12, 17]
SOB	Molybdenite	Re-Os	Metallogenic	228.3 ± 3.8, 230.0 ± 4.8	[23]
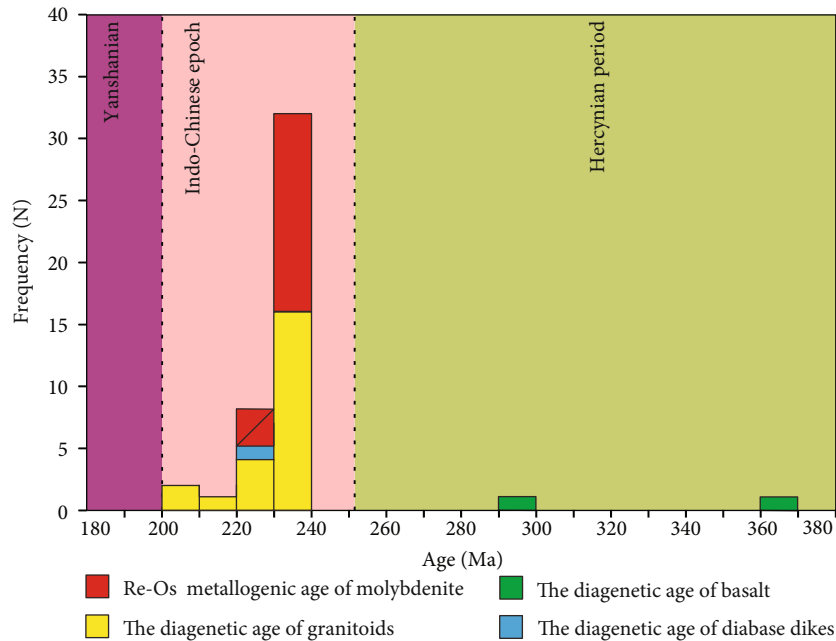
FIGURE 2: The histogram of diagenetic and metallogenic ages of the YCD, Yunnan, China.

2.64 km^2, and forms an elliptical shape [25, 27]. Dikes mainly consist of diabase dikes (222 Ma) [15] (Figure 2) and fine-grained granitic dikes, appearing as irregular dikes and stockworks filled along joints and fractures [9–12, 17, 25, 27, 32].

Based on the different ore-hosting rock types, the YCD ores can be divided into 4 types: skarn, hornfels, porphyry, and veins [8, 36]. The skarn-type ore bodies are mainly distributed in the Linong ore block, with the most typical KT2 (main ore body) and KT5 ore bodies (Figure 3), and its
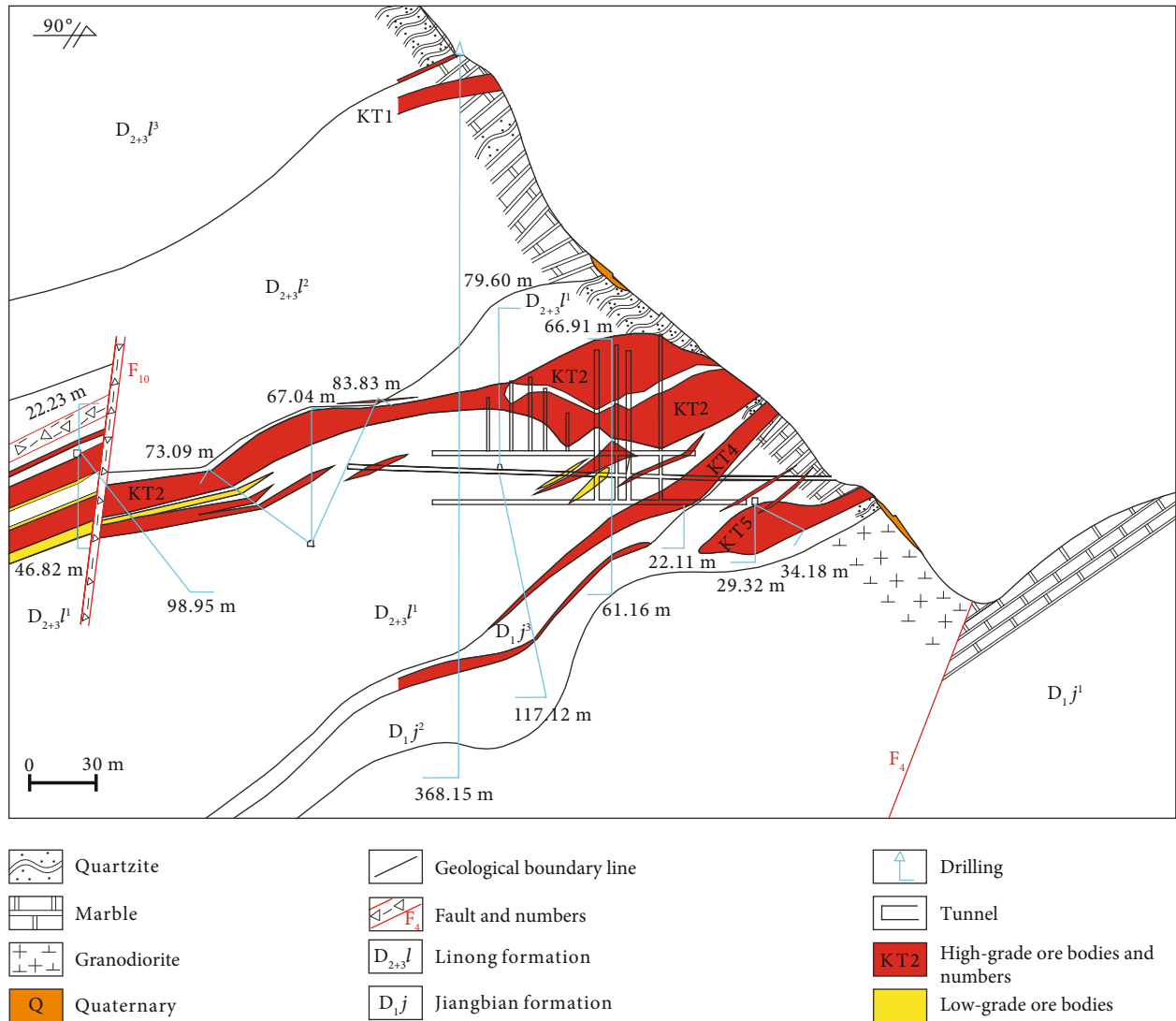
FIGURE 3: The no. 25 prospecting line profile map in the Linong ore block, YCD, Yunnan, China.

metallogenic ages are 228-235 Ma (average 230 Ma) (Table 1, Figure 2) [9–12, 16, 17, 19, 23]. The hornfel-type ore bodies are mainly distributed in the Linong and Lunong ore blocks and the hydrothermal vein-type ore bodies are mainly distributed in the Linong, Jiangbian, Tongjige, and Jiaren ore blocks. The copper ore bodies of the Linong block mainly occur in the outer contact zone between the pluton and the surrounding rock. It has a variably stratified or vein-like structure and is obviously controlled by the interlayer fracture zone. The copper ore bodies of the Lunong, Tongjige, and Jiaren ore blocks occur within the pluton and the surrounding rock and in the outer contact zone between them. Their morphology is controlled by the contact zone [34]. The upper and lower interface of the ore bodies are composed of quartzite, marble, and sericite sandy slate. The ore body is inclined toward the west with a 20-30° dip angle, and it is obviously controlled by the regional tectonic structure (Figure 3). The alteration-mineralization are mainly chalcopyrite, pyrite, pyrrhotite, galena, sphalerite, and mala-chite. Copper ores are associated with Pb, Zn, Ag, Au, As, Mo, and Sb [16]. The ore minerals are mainly chalcopyrite, pyrite, pyrrhotite, and a small amount of bornite, galena, molybdenum, sphalerite, malachite, and covellite. The gangue minerals include quartz, calcite, biotite, plagioclase, diopside, tremolite, chlorite, and garnet. The ore textures include euhedral and anhedral, metasomatic, porphyroblastic/porphyritic, crushed, and interstitial. The ore structures can be massive, disseminated, stockwork, banded, and lumpy in SOB [4, 8–12].

2.3. Characteristics of the MGP. The porphyry pluton was first found as an irregular outcrop in the Linong ore block, YCD. The stock-shaped outcrop intrudes into the Linong sericite sandy slate and quartzite [35]. The contact zones host small amounts of pyrite, galena, and magnetite. This porphyritic pluton is spatially related to the KT1 ore body of the Linong ore block, and it has been inferred to be genetically related to the porphyritic copper mineralization [35].
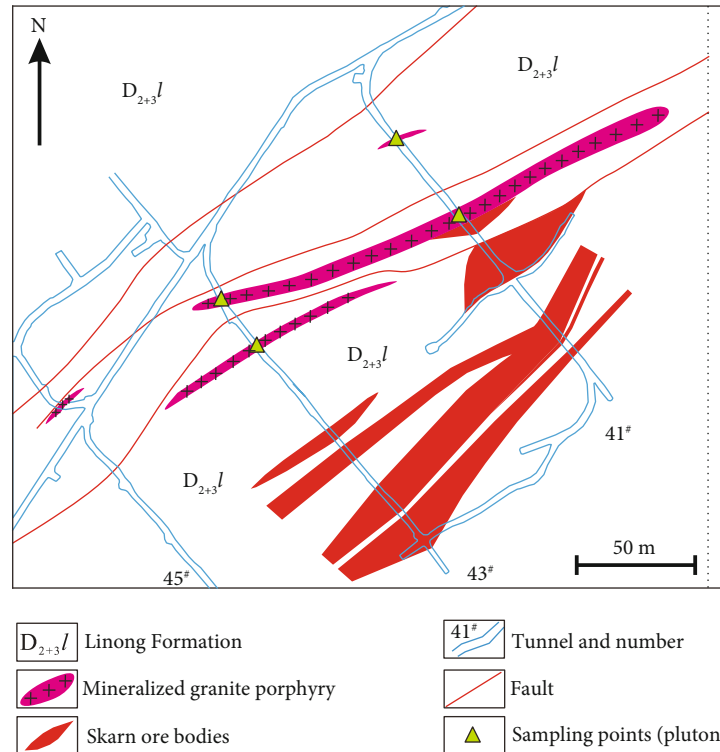
FIGURE 4: The tunnel 3250 m level geology map in the Linong ore block, YCD, Yunnan, China.

The MGP of the tunnel 3250 m level of the YCD exhibits dike-like intrusions into the sericite sandy slate and the quartzite of Linong formation ($D_{2+3}l$) (Figures 4 and 5). One dike strike 60° NE and dips 40° NW is about 4 m in width and displays an irregular contact with its host rock (Figures 5(e) and 5(g)), and there are quartz-sulfide veins and disseminated sulfides in the porphyry pluton (Figure 5(f)). The inner and outer contact zones are skarnization, silicification, sericitization, chloritization, carbonatation, pyritization, and chalcopyritization (Figures 5(a)–5(d) and 5(g)–5(h)). Furthermore, there are mainly 4 mineralization-alteration zones from SE to NW (Figure 5): Zone I: carbonatation, silicification, argillization, sericitization, and weak pyritization. Zone II: skarnization, pyritization, chalcopyritization, silicification, and carbonatation. Zone III: the mineralized granite porphyry dike with strong silicification, as well as calcitization, pyritization, chalcopyritization, molybdenitization, sericitization, and chloritization. Zone IV: silicification, pyritization, sericitization, and chloritization. The mineralization-alteration characteristics are similar to those of the typical porphyry Cu deposits.

The MGP is a gray, veinlet, disseminated, and massive structure and has a blastoporphyritic-porphyritic texture (Figures 6(a)–6(f)). The phenocryst mainly includes quartz (20%-35%), plagioclase (20%-30%), and biotite (5%-10%), and the quartz phenocryst were irregular and elliptical in shape which was developed in the MGP (Figures 6(a)–6(d) and 7(a)–7(g)). The plagioclase and biotite phenocryst had been various degrees altered (sericitization, chloritization, and carbonatation) (Figures 7(d)–7(g)). The phenocryst of

quartz, plagioclase, and biotite were shown to be subeuhedral to euhedral granular, corroded, board-shaped, and fissile textures (Figures 7(a)–7(g)). The plagioclase and biotite phenocryst were completely/partly replaced by sericite, chlorite, and cryptocrystalline carbonate minerals and experienced various degrees of sericitization, chloritization, carbonation, argillization, and silicification (Figures 7(d)–7(g)). The matrix is composed of quartz and plagioclase and minor biotite, with cryptocrystalline, microcrystalline, and felsitic textures (Figures 7(a)–7(g)). Accessory minerals include zircon, sphene, and apatite. Furthermore, a large number of vein-reticulate vein quartz (Figures 6(e) and 6(f)) and a few of vein-disseminated sulfides (pyrite, chalcopyrite, and bornite) have developed in the MGP (Figures 6(a), 6(b), 6(e) and 6(f)). The quartz phenocryst is cut through by quartz-sulfide veins (Figures 7(h)–7(j)), and it shows that quartz-sulfide veins were formed later the post-diagenetic. Besides, the calcite veins cut through quartz phenocryst and quartz-sulfide veins, indicating that calcite veins formed quartz-sulfides veins and quartz phenocryst later (Figures 7(j) and 7(k)). To sum up, the mineral formation sequence was quartz phenocryst→quartz, pyrite, chalcopyrite→calcite.

The MGP (porphyry ores) shows a veined, banded, and massive structure (Figures 6(g)–6(r)). Moreover, a large number of pyrite, chalcopyrite (Figures 6(g)–6(r) and 7(l)–7(r)), bornite (Figures 6(h)–6(i)), sphalerite (Figure 7(r)), quartz (Figures 6(g)–6(k), 6(m)–6(q), and 7(l)–7(r)), and calcite (Figures 6(o)–7(l)) developed in the MGP. The pyrite and chalcopyrite are veinlets with irregular shape, massive, and disseminated; the sphalerite are irregular shaped; and the

FIGURE 5: The sketch map of 41#-1 mining stope at a 3250 m level in the YCD, Yunnan, China. 1-quartzite, 2-sericite slate, 3-MGP, 4-calcite veins, 5-quartz veins, 6-sulfide veins, 7-sample and numbers, 8-photos, 9-low-grade SOB, 10-High-grade SOB, 11-mineralization-alteration zone. (a) The strongly silicified quartzite, which developed the veins, scattered, and disseminated pyrite. (b) The low-grade SOB, which developed disseminated pyrite and chalcopyrite and later calcite vein. (c) The sericite slate, which developed partially disseminated pyrite and later calcite vein. (d) The high-grade SOB and developed disseminated pyrite and chalcopyrite. (e) The irregular contact line of the MGP and SOB, which developed a large number of quartz veins in the MGP. (f) The MGP, which developed vein-disseminated metal sulfides (pyrite, chalcopyrite, bornite, and molybdenite) and quartz veins. (g) The irregular contact line of the MGP and sericite slate, which developed veins metal sulfides in the MGP, and there are many quartz veins in the sericite slate of Linong formation. (h) The sericite slate, which developed the later quartz veins, disseminated-fine vein metal sulfides. Zone I: carbonatation, silicification, argillization, sericitization, and weak pyritization. Zone II: skarnization, pyritization, chalcopyritization, silicification, and carbonatation. Zone III: the mineralized granite porphyry dike with strong silicification, as well as calcitization, pyritization, chalcopyritization, molybdenitization, sericitization, and chloritization. Zone IV: silicification, pyritization, sericitization, and chloritization.

quartz-calcite are veined. Additionally, within the quartz veins, a large amount of veinlet and disseminated pyrite, chalcopyrite, and a smaller amount of sphalerite have developed (Figures 7(l)–7(r)) by metasomatism in the pores and microfissures of the host rock and the quartz veins, assuming anhedral-granular, scattered-disseminated, and irregular veinlet growth. Chalcopyrite intersects and replaces pyrite indicating that chalcopyrite developed after the pyrite (Figures 7(o)–7(r)). Sphalerite intersected and replaced chalcopyrite and pyrite, indicating that sphalerite was formed later than chalcopyrite and pyrite (Figure 7(r)). Thus, the mineral paragentic associatons can be summarized as pyrite→chalcopyrite→sphalerite within the quartz veins in the hydrothermal mineralization periods and the mineral assemblage were mainly quartz-pyrite-chalcopyrite-sphalerite.

To sum up, based on the observation of macroscopic and microscopic characteristics of the minerals in the MGP samples (Figures 6 and 7), diagenesis-mineralization can be divided into three stages from diagenesis to hydrothermal mineralization, such as (i) the diagenesis stage and quartz, plagioclase, and biotite phenocryst crystallized out of granitoid magma and formed granite porphyry; (ii) quartz-sulfide stage, forming a large number of quartz-sulfide veins (quartz, pyrite, chalcopyrite, sphalerite, bornite, etc.) and representing hydrothermal mineralization and forming porphyry (mineralization) ore bodies within the granite porphyry (pluton); and (iii) the calcite stage, the formation of a large number of nonmetallic mineralization of calcite veins, representing the hydrothermal mineralization has ended.

3. Materials and Methods

The MGP samples used for the analyses of fluid inclusions and H-O-S-Pb isotopes were obtained from the tunnel

(a)

(b)

(c)

(d)

(e)

(f)

(g)

(h)

(i)

(j)

(k)

(l)

(m)

(n)

(o)
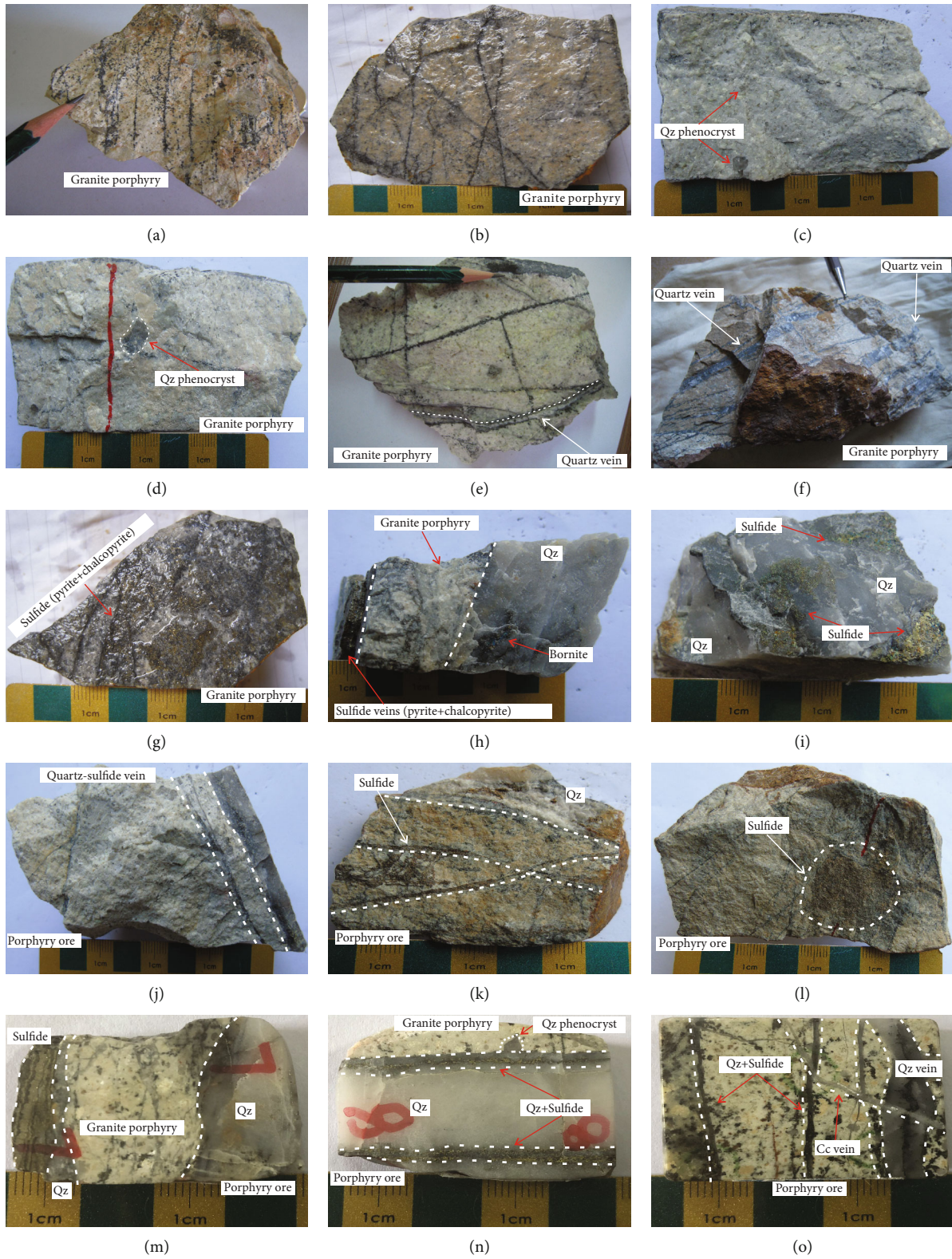
Figure 6: Continued.
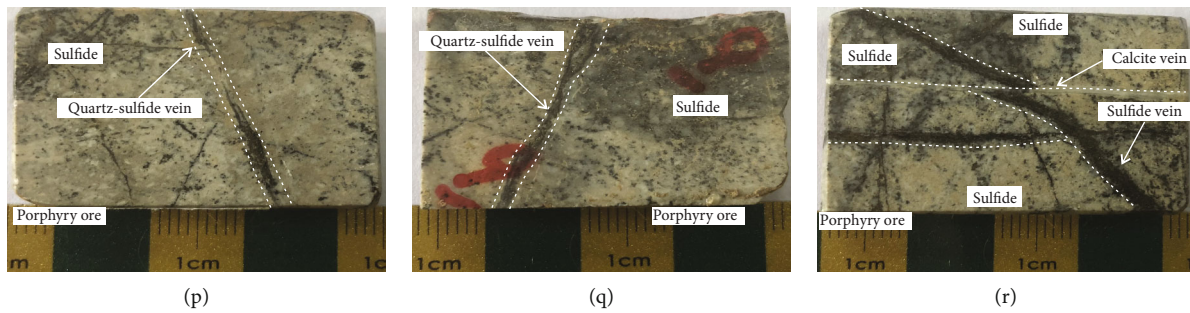
FIGURE 6: The photographs of the MGP in the YCD, Yunnan, China. (a) The light-offwhite massive structure granitic porphyry,which developed fine vein-spotted metal sulfides (Sample No.YM-2). (b) The light-offwhite massive structure granite porphyry, which developed a large number of fine vein metal sulfides (Sample No. 41-1). (c) The offwhite massive structure granite porphyry, the quartz phenocryst have hypidiomorphic-panidiomorphic texture and isometric texture, and the plagioclase are strongly altered and present a dissolution texture (Sample No. 41-2). (d) The offwhite massive structure granite porphyry, and the quartz phenocryst are elliptical in shape (Sample No. YM-3). (e) The gray massive structure MGP, which developed fine-veined pyrite and chalcopyrite and quartz vein (Sample No. YM-4). (f) The gray massive structure MGP, which developed a large number of quartz vein (Sample No. YM-5). (g) The massive structure MGP (porphyry ore), which developed a large number of disseminated, fine-veined pyrite and chalcopyrite (Sample No. 41-3). (h) The massive structure MGP (porphyry ore), which developed veins of metal sulfides (pyrite, chalcopyrite), quartz, and disseminated bornite (Sample No. 3250-41-5). (i) The massive structure quartz, which developed disseminated metal sulfides (pyrite, chalcopyrite, and bornite) (Sample No. 3250-41-5). (j) The massive structure MGP (porphyry ore), which developed veinlets of metal sulfides (pyrite, chalcopyrite) and quartz (Sample No. 41-1). (k) The massive structure MGP (porphyry ore), which developed veinlets and disseminated metal sulfides (pyrite, chalcopyrite) and quartz (Sample No. 41-2). (l) The massive structure MGP (porphyry ore), which developed disseminated metal sulfides (pyrite, chalcopyrite) and quartz (Sample No. 41-3). (m) The veins of quartz and sulfide are developed in MGP (porphyry ore) (Sample No. 41-1). (n) The parallel veins of quartz and sulfides are developed in MGP (porphyry ore), and the quartz phenocryst was penetrated by late quartz-sulfide parallel veins (Sample No. 41-2). (o) The early quartz-sulfide veins were cut/penetrated by later calcite vein, showing the evolution trend from quartz-sulfide veins to calcite vein in MGP (porphyry ore) (Sample No.3275-39). (p, q) The massive structure MGP (porphyry ore), which developed veinlets and disseminated metal sulfides (pyrite, chalcopyrite) and quartz (Sample No. 41-3). (r) The massive structure MGP (porphyry ore), which developed veinlets and disseminated metal sulfides (pyrite, chalcopyrite), quartz, and later calcite vein (Sample No. 41-4). Qz-quartz, Cc-calcite, Pl-plagioclase, Bi-biotite, Py-pyrite, Ccp-chalcopyrite, Sp-sphalerite.

3250 m level of the 41 mine, Linong ore block, YCD. Some quartz-sulfide ores that precipitated during the stage of hydrothermal mineralization were collected from the Linong ore block for fluid inclusions and detailed isotope analysis. From these ores, 11 and 4 ore-bearing quartz samples were collected for fluid inclusions and oxygen and hydrogen isotope analyses, respectively. 10 and 13 sulfide samples were collected for sulfur and lead isotope analysis.

3.1. Fluid Inclusions. The ore sample characteristics of fluid inclusions are summarized as follows: Sample No. YM-1: the gray-white massive porphyry Cu ore. Sulfides are vein-like and partially irregular and the quartz are vein-like. Quartz and sulfide veins have a symbiotic relationship and sulfides are partially developed clusters within the quartz veins (Figure 8(a)). Sample No. YM-2: the gray massive quartz, developing disseminated metallic sulfides (pyrite, chalcopyrite, and bornite), and there is a symbiotic relationship between quartz and metallic sulfides (Figure 8(b)). Sample No. YM-5: the gray massive porphyry Cu ore. Pyrite and chalcopyrite are vein-web-like and partially disseminated, and the quartz are vein-like and irregularly agglomerated (Figure 8(c)). Sample No. YM-7: the gray-white massive quartz with fine veins and clusters of metal sulfides (Figure 8(d)). Sample No. YM-8: the gray-white massive quartz with fine veins pyrite and chalcopyrite (Figure 8(e)). Sample No. YM-9: the gray massive porphyry type Cu ore,

and the quartz and metal sulfides have a vein symbiotic relationship (Figure 8(f)).

The microthermometric and Laser Raman analyses of the fluid inclusions were performed at the fluid inclusion laboratory of the Kunming University of Science and Technology. The analyses were conducted using a Linkam THMS600 heating/freezing stage. The testing temperature ranged from -196 to 600°C, with a homogenization temperature measurement error of ±2°C and an ice melting temperature measurement error of ±0.2°C. The heating and the cooling rates began at 30°C/min and were reduced to both 1°C/min and 0.5°C/min close to the phase transition point. Each inclusion sample was subjected to heating and freezing, and in each scenario, each sample was measured twice or more to check the precision of the temperature measurements and to ensure that no leaks had occurred. A Renishaw 2000 Raman Imaging Microscope was used for Laser Raman analyses. The laser has a wavelength of 514.53 nm with a power of 20 mW, a minimum laser beam spot diameter of 1 μm, and a spectral resolution of 1-2 cm^{-1}.

The petrography and temperature measurements of fluid inclusions were conducted in quartz. At room temperature, the fluid inclusions were mostly gas-liquid two-phase inclusions, followed by monophase liquid inclusions (Figure 9). Primary inclusions exhibited strip-like, elliptical, spherical, and irregular shapes, with variably scattered and dense distributions. In some areas, visible secondary fluid inclusions,
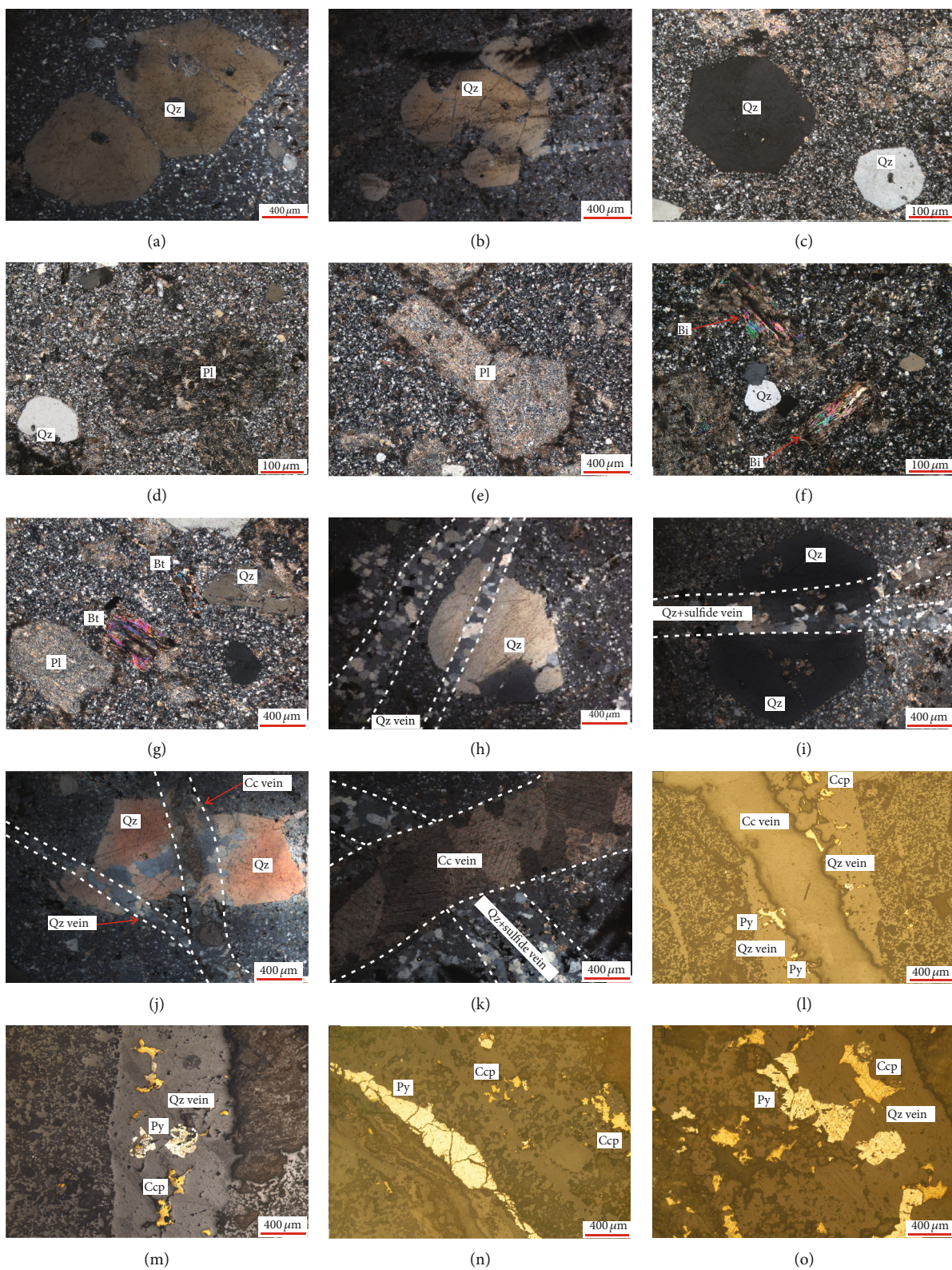
(a)

(b)

(c)

(d)

(e)

(f)

(g)

(h)

(i)

(j)

(k)

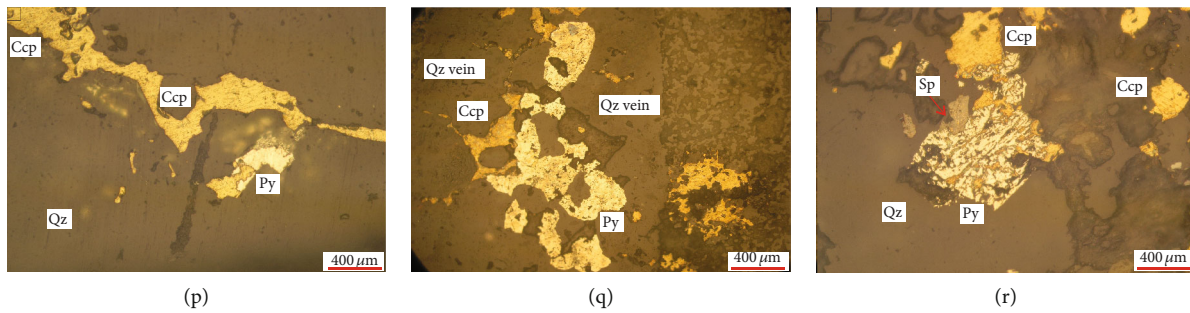(l)

(m)

(n)

(o)

Figure 7: Continued.

(p)

(q)

(r)

Figure 7: Photomicrographs of the MGP in the YCD, Yunnan, China. (a)The quartz phenocryst are panidiomorphic-isometric texture, and dissolution texture in granite porphyry (+) (Sample No. 3275-39). (b) The quartz phenocryst are irregular and embayment shape in granite porphyry (+) (Sample No. 41-3). (c) The porphyritic texture granite porphyry, the phenocryst are panidiomorphic-isometric texture, dissolution texture quartz, and the matrix is a microgranular texture feldspar-quartz (+) (Sample No. 41-3). (d) The porphyritic texture granitic porphyry, the phenocryst are hypidiomorphic-isometric texture, dissolution texture quartz and sericitization plagioclase, the matrix is a microgranular texture feldspar-quartz (+) (Sample No. 3250-41Lb3). (e) The irregular and embayment shape, dissolution texture sericitization plagioclase in granite porphyry (+) (Sample No. 41-1). (f) The porphyritic texture granitic porphyry, the phenocryst are hypidiomorphic-isometric texture, dissolution texture quartz and biotite, the matrix is a microgranular texture feldspar-quartz (+) (Sample No. 45-R4-2). (g) The porphyritic texture granitic porphyry, the phenocryst are hypidiomorphic-isometric texture, dissolution texture quartz, sericitization plagioclase, and biotite, the matrix is a microgranular texture feldspar-quartz (+) (Sample No. 41-1). (h) The quartz veins cut/penetrated the quartz phenocryst, and the evolution sequence from quartz phenocryst to quartz veins is shown (+) (Sample No. 3275-41b1). (i) The quartz-sulfide veins cut/penetrated the quartz phenocryst, and the evolution sequence from quartz phenocryst to quartz - sulfide veins is shown (+) (Sample No. 3250-41b3). (j) The calcite veins cut/penetrated the quartz vein and quartz phenocryst, and the quartz vein cut/penetrated the quartz phenocryst. The evolution sequence of quartz phenocryst→quartz veins→calcite veins is shown (+) (Sample No. 3250-41b3). (k) The calcite vein cut/penetrated quartz-sulfides vein, and showing the evolution sequence from quartz-sulfide vein to calcite vein (+) (Sample No. 3275-39). (l) The chalcopyrite and pyrite are scattered along the quartz vein, and chalcopyrite, pyrite, quartz vein are replaced by later calcite vein (-) (Sample No. 3275-39). (m) The irregular pyrite and chalcopyrite developed in quartz vein (-) (Sample No. 3275-39). (n) The pyrite is fine-veined, and chalcopyrite is scattered in the MGP (-) (Sample No. 3275-41-b1). (o) The xenomorphic granular texture pyrite and chalcopyrite are disseminated with scattered and irregular veins that are developed along the fissure-fine fissures in the granitic porphyry, and the pyrite is replaced by the chalcopyrite (-) (Sample No. 3275-39). (p) The chalcopyrite and pyrite are filled with quartz vein fissures, and the xenomorphic granular texture pyrite are replaced by the chalcopyrite (-) (Sample No. 3275-41b1). (q) The chalcopyrite and pyrite are developed in quartz vein fissures, and the pyrite is replaced by the chalcopyrite (-) (Sample No. 3250-41-5). (r) The pyrite is replaced by granule chalcopyrite along the fissure, and the pyrite presented skeleton texture. The pyrite and chalcopyrite are replaced by irregular shape sphalerite (-) (Sample No. 3250-39). Qz-quartz, Cc-calcite, Pl-plagioclase, Bi-biotite, Py-pyrite, Ccp-chalcopyrite, Sp-sphalerite.

mainly with strip-like, elliptical, spherical, and irregular morphologies, assumed linear distributions along fractures. In this study, all of the measured fluid inclusions were of primary phases. The primary inclusions were of two types: (1) enriched liquid-phase inclusions (V-L), which constituted ~96% of the total number of inclusions. At room temperature, a gas-liquid two-phase composition was observed (Figures 9(a)–9(f)). Their size ranged from 4-12 μm, with most having between 4 and 7 μm diameter. Morphologies were most often elliptical, spherical, strip-like, and irregular. Inclusions were heated uniformly until they reached a liquid phase (2), monophase liquid inclusions (L), which constituted 4% of the total number of inclusions. The inclusion ranged in size from 4 to 6 μm, with small sizes being more common. Most inclusions were elliptical or irregular in shape (Figures 9(a)–9(c)).

3.2. H-O Isotopes. Analyses of hydrogen and oxygen isotopes in quartz (hydrothermal) were completed at the Laboratory of Isotope Geology of the Institute of Geology of the Chinese Academy of Geological Sciences. Hydrogen and oxygen isotopes of quartz were analyzed using a Finningan MAT 253 mass spectrometer. The sample preparation process is as follows: firstly, the samples are broken and pure quartz particles (40 mesh) are selected by handpicking under binocular microscope, and the quartz particles are crushed into powder. The conventional BrF_5 method was used for oxygen isotope analysis of quartz, and BrF_5 was used to react with oxygen-containing minerals in vacuum and high temperature to extract mineral oxygen, which was then burned with a hot resistance-graphite and converted into CO_2 gas [37]. Hydrogen isotopes of quartz inclusions were opened by vacuum thermal explosion method, the water was obtained by separation, and water was reacted with zinc to obtain H_2 gas for mass spectrometry [38]. The oxygen isotopes and inclusion hydrogen isotope analysis of quartz determination precision were ± 2‰, and the analytical results were reported relative to the SMOW ("Standard Mean Ocean Water") standard.

3.3. S Isotopes. Sulfur isotope analyses were conducted at the Laboratory of Isotope Geology of the Institute of Geology of the Chinese Academy of Geological Sciences. The sulfide-bearing rock samples were mechanically crushed and the pyrite and chalcopyrite were separated by handpicking under the microscope. Single grains of pyrite and chalcopyrite were mixed with copper oxide (CuO), heated and oxidized, and

(a)

(b)

(c)

(d)

(e)

(f)
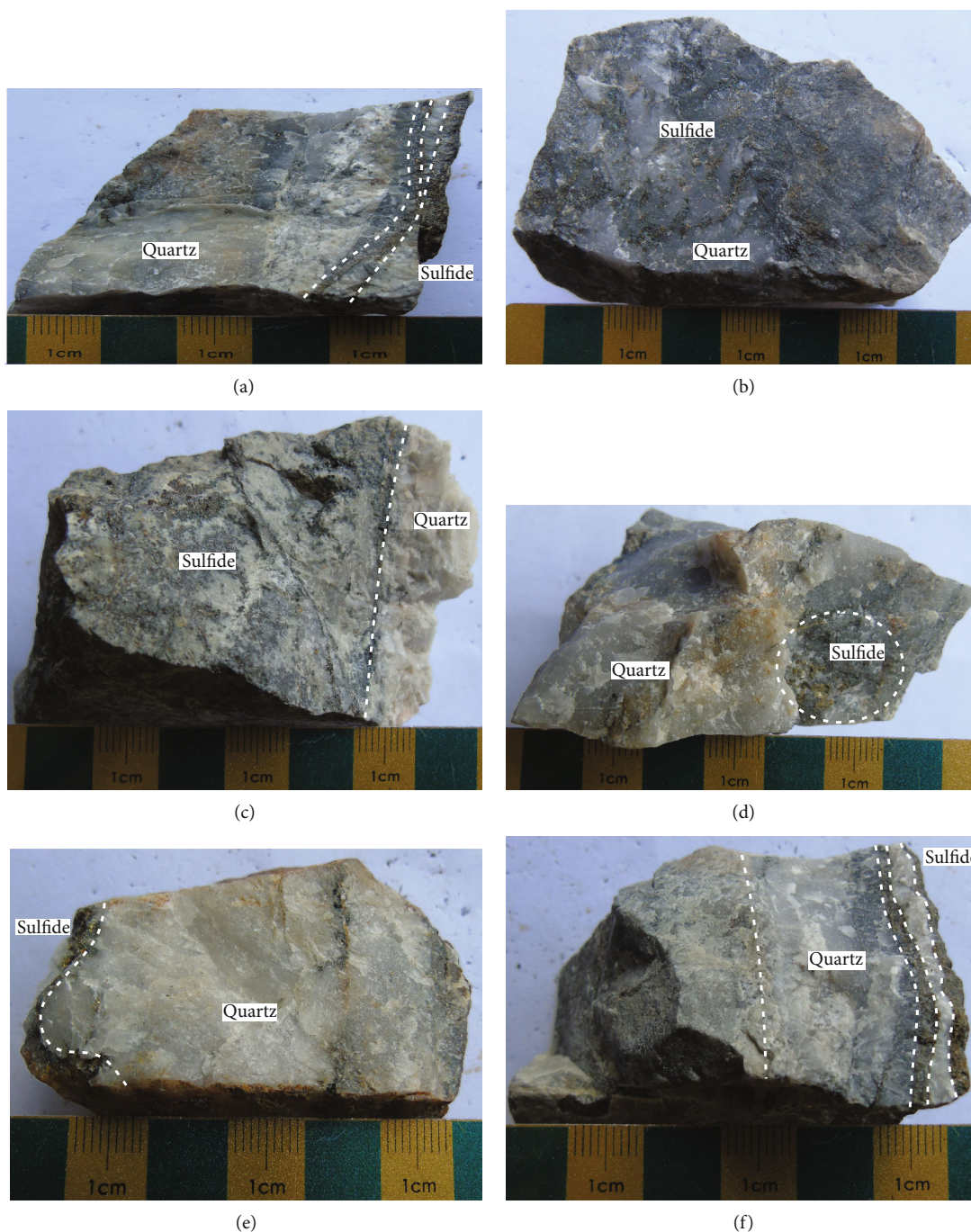
Figure 8: The photos of porphyry ore specimens,YCD, Yunnan, China (Sample No. (a) YM-1, (b) YM-2, (c) YM-5, (d) YM-7, (e) YM-8, and (f) YM-9).

formed SO_2 gas. The generated SO_2 gas was frozen and extracted using the method of liquid nitrogen. The sulfur isotope composition was analyzed by the collected SO_2 gas using a MAT 251 Mass Spectrometer. The results are reported with respect to the V-CDT standard with a precision of ±0.2‰.

3.4. Pb Isotopes. Lead isotope analyses were performed at the Laboratory of Isotope Geology of the Institute of Geology of the Chinese Academy of Geological Sciences. The Pb

separation and purification was achieved using used AG1-X8 anion exchange resin. The analyses were performed using a Nu Plasma HR high-resolution multicollector inductively coupled plasma mass spectrometer. The mass fractionation of the instrument was externally corrected using about one-half the lead content of the samples of T1 isotope standard [39]. A NBS 981 standard was used to monitor the results, with values of $^{208}Pb/^{206}Pb = 2.16736 \pm 0.00066$ (2σ), $^{207}Pb/^{206}Pb = 0.91488 \pm 0.00028$, $^{206}Pb/^{204}Pb = 16.9386 \pm$
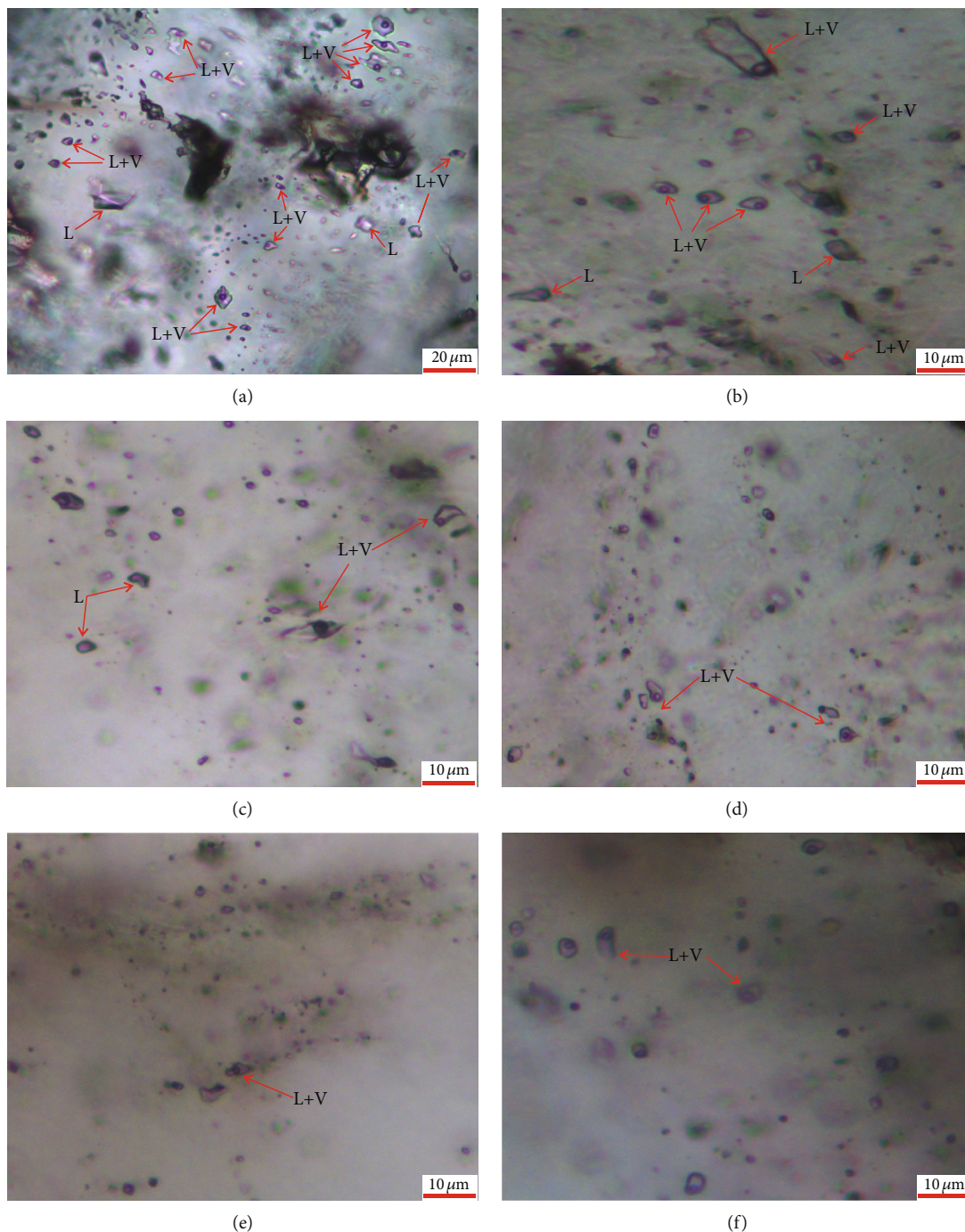
FIGURE 9: Microphotographs of typical fluid inclusions in the MGP, YCD, Yunnan, China. L+V: gas-liquid fluid inclusions; L: liquid fluid inclusions (Sample No. (a) YM-1, (b) YM-2, (c) YM-5, (d) YM-7, (e) YM-8, and (f) YM-9).

0.0131, $^{207}Pb/^{204}Pb = 15.4968 \pm 0.0107$, and $^{208}Pb/^{204}Pb = 36.7119 \pm 0.0331$. The accuracy of $^{208}Pb/^{204}Pb$ for $1 \mu g$ is ≤0.005%.

4. Results

4.1. Fluid Inclusions

4.1.1. Microthermometry. During petrographic observation of the fluid inclusions from the MGP, no carbon dioxide-containing or crystalline inclusions were discovered. Therefore, in this study, the ice melting temperature (T_m) and homogenization temperature (T_h) were only determined for gas-liquid two-phase inclusions (>$4 \mu m$). Moreover, the results of previous analyses on fluid inclusions in garnet, epidote, pyroxene, quartz, and calcite from the SOB of this deposit were also considered [17, 24–26].

The corresponding salinities of the fluid inclusions were calculated based on the salinity equation of Lu et al. [40], i.e., $W = 0.00 + 1.78T_m - 0.0422T_m^2 + 0.000557T_m^3$. The fluid

(a)

(b)

(c)

(d)
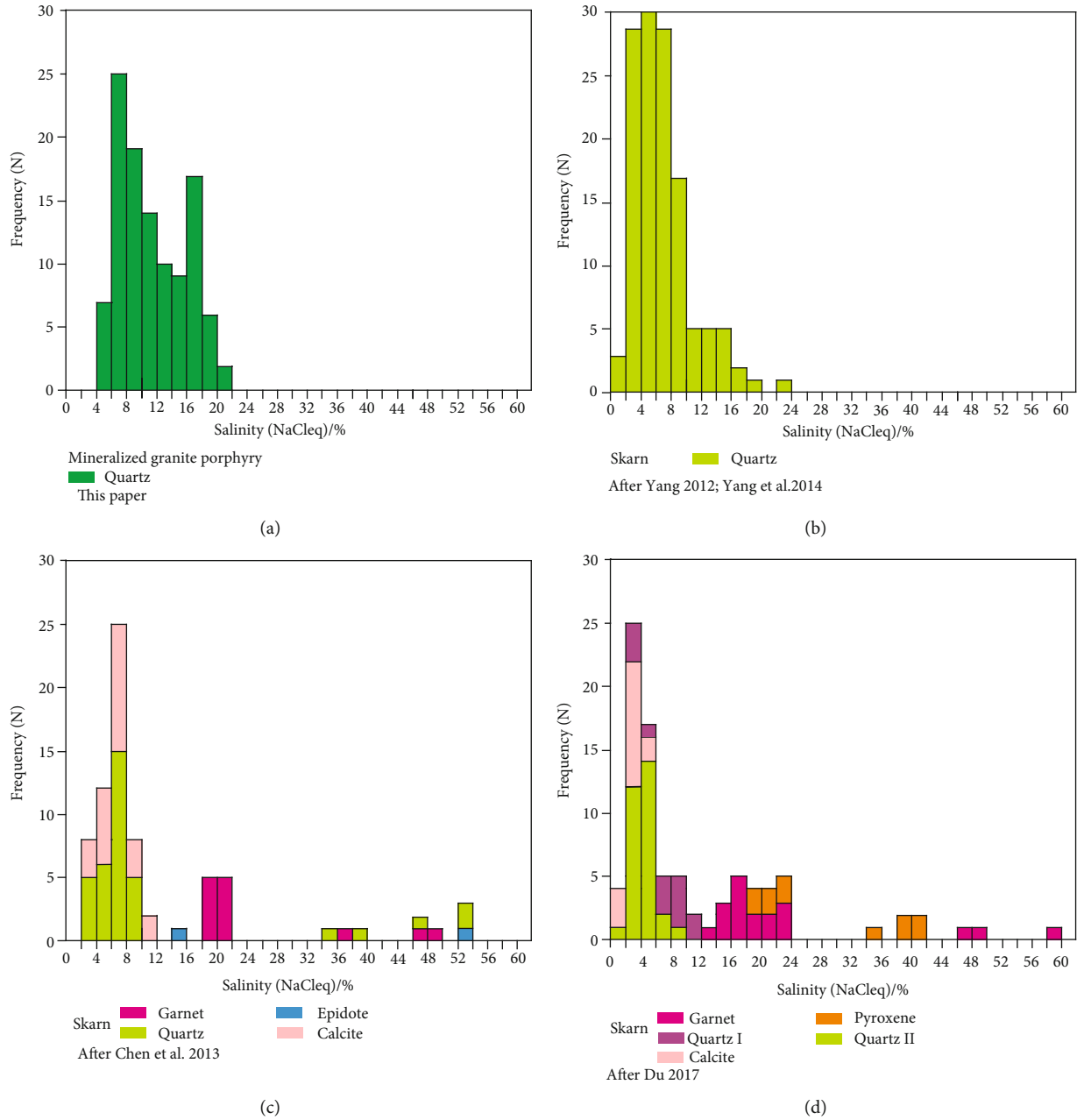
FIGURE 10: The salinities of the fluid inclusions in the MGP (a) and SOB (b–d), YCD, Yunnan, China.

inclusion density was determined from homogenization temperature-salinity-density phase diagrams (Figure 10) and the entrapment pressure was estimated from homogenization temperature-salinity-pressure phase diagram in the H_2O-NaCl system [24, 41–43].

The fluid inclusions were divided into two categories based on T_h (127°C to 316°C) and salinities (4 to 21 wt.% $NaCl_{eq}$): (1) low temperature-low salinity fluid inclusions and (2) medium temperature-medium salinity fluid inclusions (Table 2, Figures 10(a) and 11(a)).

For fluid inclusions of the 1st group, the variation in T_m ranged from -16°C to -2°C (average 7°C). T_h ranged from 127°C to 207°C but most data were concentrated between

160°C and 200°C (average 168°C). Based on the salinity equation [40, 44], salinity ranged from 4 to 19 wt.% $NaCl_{eq}$ (average 10 wt.% $NaCl_{eq}$) was calculated. Based on the density and isochoric formulae for NaCl-H_2O [45–47], a fluid density of 0.9 to 1.07 g/cm^{-3} (average 0.98 g/cm^{-3}) was calculated(Figure 12(a)). The entrapment pressure was estimated to range from 6 to 12 bars (average 8 bars) (Figure 13(a)).

For fluid inclusions of the second group, the variation in T_m ranged from -18°C to -10°C (average -13°C) and T_h ranged from 283°C to 316°C and was mainly concentrated between 280°C and 320°C (average 300°C). The salinity ranged from 14 to 21 wt.% $NaCl_{eq}$ (average 17 wt%.

Table 2: The tested and calculated data of fluid inclusions from the mineralized granitic porphyry (MGP) and skarn ore bodies (SOB), Yangla copper deposit, Yunnan, China.

Sample	Minerals	Type	T_h (homogenization) (°C) Range/number	Average	Mt (melting temperature of NaCl crystal) (°C) Range/number	Average	T_m (ice melting) (°C) Range/number	Average	Salinity (ω NaCleq) Range/number	Average	Density (g·cm⁻³) Range/number	Average	Pressure (bars) Range/number	Average	References
MGP	Quartz	V-L	127~207/100	175	—	—	-2~-16/100	-10	4~19/100	10	0.90~1.07/100	0.98	6~12/100	8	This paper
		V-L	283~316/10	300	—	—	-18~-10/10	-13	14~21/10	17	0.85~0.95/10	0.89	50~100/10	80	
	Quartz	V-L	120~336/95	—	—	—	-0.20~-19.50/95	—	0.35~22.03/95	—	0.69~1.08/95	—	5~120/95	12	[17, 26]
		V-L	413~543/9	468	—	—	-19~-15/9	-17.8	19~22/9	20	0.65~1.07/9	0.75	250~590/12	400	
	Garnet	S-V-L	—	—	292~423/3	372	—	—	37~49/3	44	0.9~1.0	1.0			
	Epidote	V-L	336~498	415	—	—	-11/1	-11	15.7/1	15	0.8	0.8	120~320/2	220	[25]
		S-V-L	—	—	452/1	452	—	—	53/1	53	1.0	1.0			
	Quartz	V-L	148~331/154	269	—	—	-7~-1	-3	2~9	6	0.7~1.0	0.8	8~120	30	
		S-V-L	—	—	262~539/7	425	—	—	35~65/7	51	1.0	1.0			
SOB	Calcite		132~179	155	—	—	-6~-2/24	-4	3~10/24	7	0.9~1.0	0.9	7~9	8	
	Garnet	V-L	372~499/18	453	—	—	-21~-9	15	13~23	18	0.5~0.8	0.6	180~500	410	
		S-V-L	499/1	499	397~492/3	437	—	—	46~58	51	1.3	1.3			[24]
	Pyroxene	V-L	366~492/16	431	—	—	-20~-15/6	-18	19~23	21	0.7~0.8	0.7	190~500	400	
		S-V-L	379~481/4	439	273~341/5	319	—	—	36~41	39	1.0	1.0			
	Quartz/I	V-L	301~415/21	351	—	—	-8~-1/13	-5	2~11	7	0.5~0.8	0.7	80~200	150	
	Quartz/II	V-L	165~294/31	238	—	—	-5~-1/26	-2	1~8	4	0.7~0.9	0.8	8~90	40	
	Calcite	V-L	142~283/18	185	—	—	-3~-1	-1	1~4	2	0.7~0.9	0.8	7~70	20	

(a)

(b)

(c)

(d)
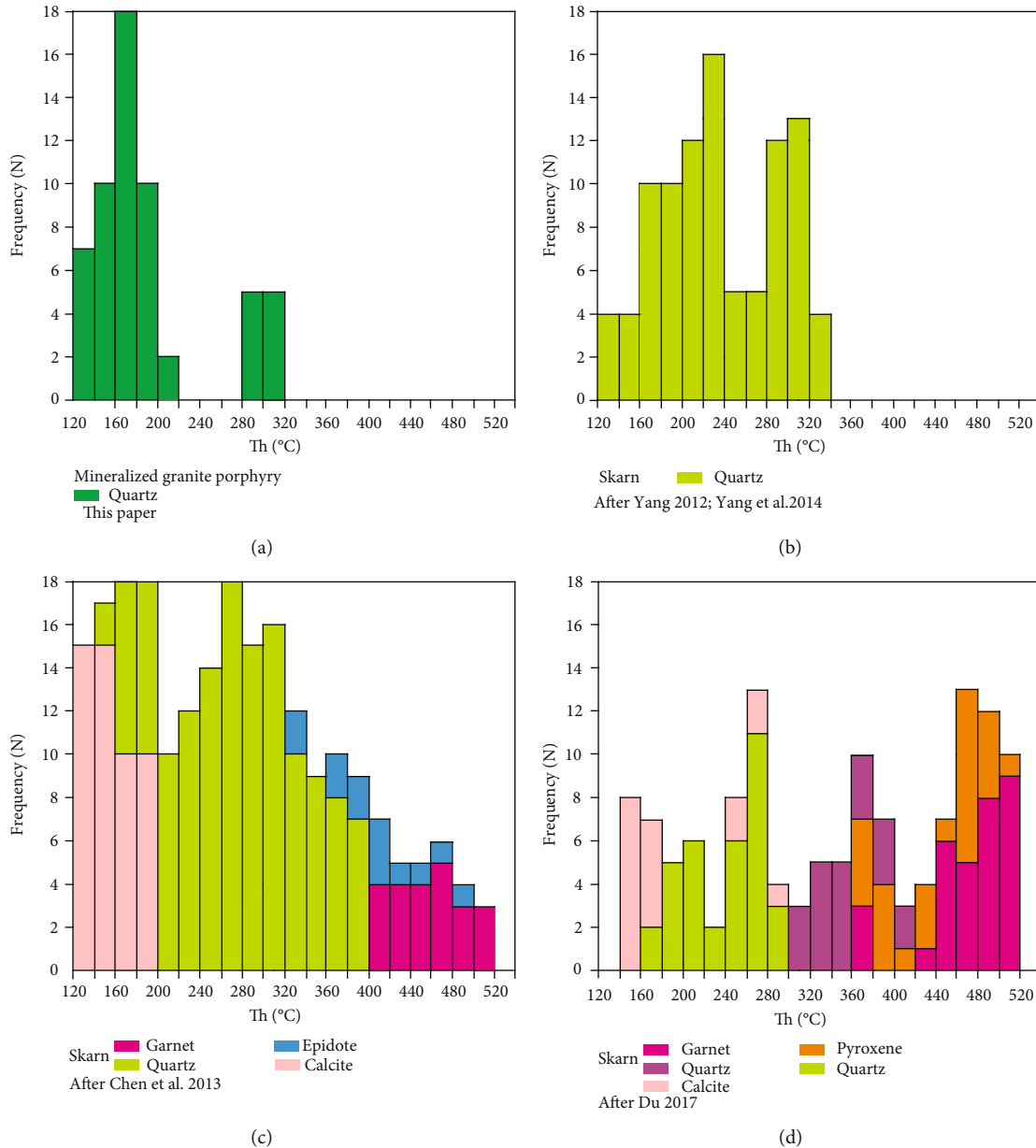
FIGURE 11: Homogenization temperatures of the fluid inclusions in the MGP (a) and SOB (b), YCD, Yunnan, China.

$NaCl_{eq}$). Based on the density and isochoric formula for the $NaCl$-H_2O system [45–47], the density ranged from 0.85 to 0.95 g/cm^{-3} with an average of 0.89 g/cm^{-3} (Figure 12(a)). A range of trapping pressures ranging from 50 to 100 bars was calculated, with an average of 80 bars (Figure 13(a)).

In fluid inclusions of the SOB (Table 2), Yang [17] and Yang et al. [26] reported that the fluid inclusions of T_m varied from -20°C to 0.2°C, T_h mainly concentrated between 200°C to 240°C and 280°C to 320°C (Figure 11(b)), the salinity ranged from 0.35 to 22 wt.% $NaCl_{eq}$ (Figure 10(b)), the density ranged from 0.7 to 1.08 g/cm^{-3} (Figure 12(b)), and the trapping pressures were estimated to range around 5 to 120 bars in quartz (Figure 13(b)). Chen et al. [25] reported the fluid inclusions of garnet, epidote, quartz, and calcite T_m var-

ied from -19°C to -15°C, -11°C, -7°C to -1°C, and -6°C to -2°C, respectively. T_h ranged from 413 to 593°C, 336°C to 498°C, 148°C to 331°C, and 132°C to 179°C, respectively (Figure 11(c)). The salinity ranged from 19 to 22 wt.% $NaCl_{eq}$, 15.7 wt.% $NaCl_{eq}$, 2 to 9 wt.% $NaCl_{eq}$, and 3 to 10 wt.% $NaCl_{eq}$, respectively (Figure 10(c)). The density ranged from 0.7 to 1.07 g/cm^{-3}, 0.83 to 1.08 g/cm^{-3}, 0.5 to 0.95 g/cm^{-3}, and 0.93 to 1.10 g/cm^{-3}, respectively (Figure 12(c)). The trapping pressures were estimated to range around 250 to 590 bars, 120 to 320 bars, 8 to 120 bars, and 7 to 9 bars, respectively (Figure 13(c)). The results show that homogeneous temperature (T_h), salinity, and trapping pressure have obviously decreased from garnet, epidote, quartz, and calcite. Du [24] reported that the fluid inclusion of garnet, pyroxene, quartz/I, quartz/II, and calcite T_m varied

(a)

Mineralized granite porphyry
▲ Quartz
This paper

(b)

Skarn ▲ Quartz
After Yang 2012; Yang et al.2014

(c)

Skarn ■ Garnet ● Epidote
▲ Quartz ◆ Calcite
After Chen et al. 2013

(d)

Skarn ■ Garnet ▲ Pyroxene
▲ Quartz I ● Quartz II
◆ Calcite
After Du 2017
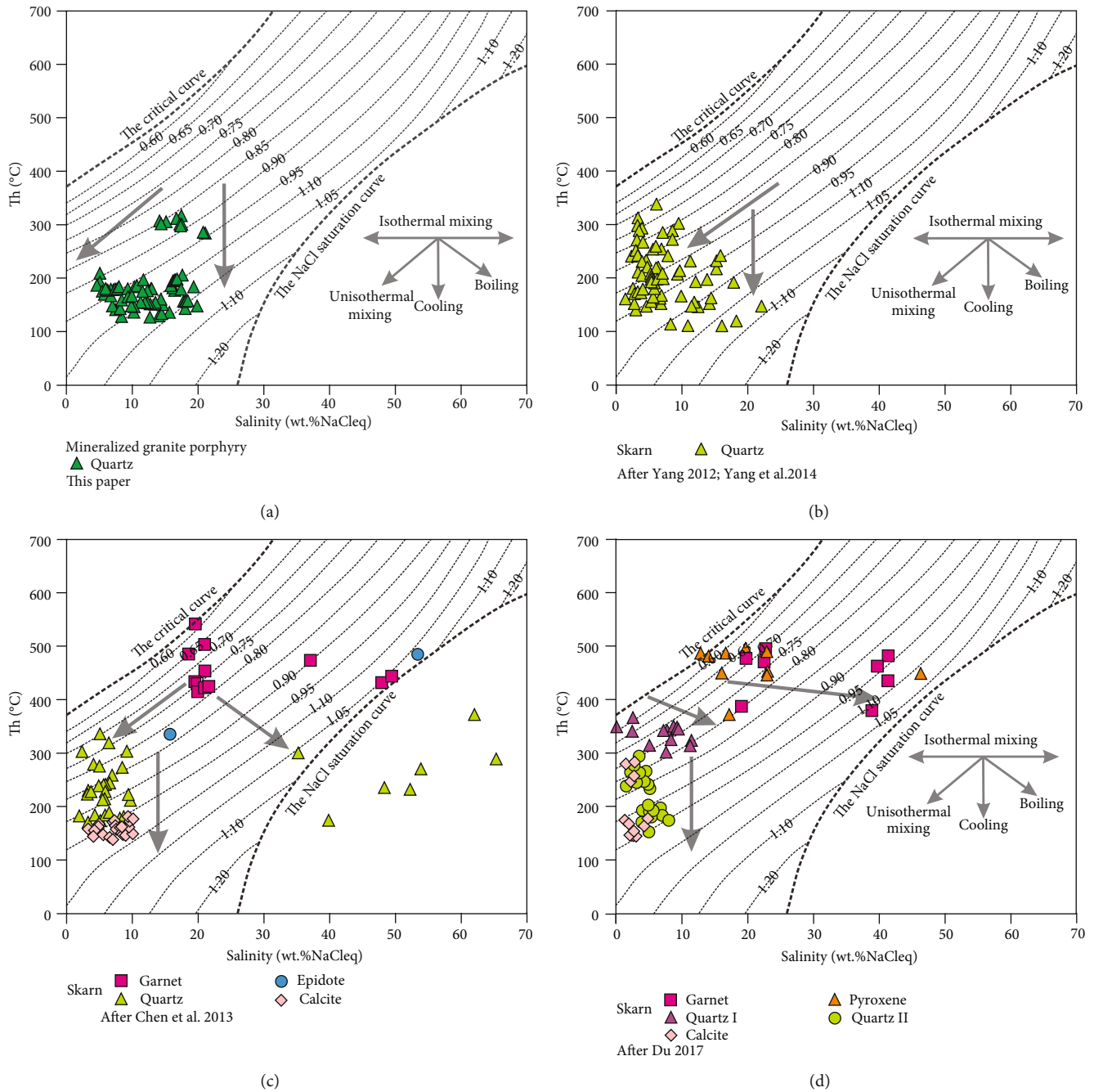
FIGURE 12: Scatter plot of salinities and homogenization temperatures of the MGP (a) and SOB (b–d), YCD, Yunnan, China.

from -21°C to -9°C, -20 to -15°C, -8°C to -1°C, -5°C to -1°C, and -1°C to -1°C, respectively. T_h ranged from 372 to 499°C, 366°C to 492°C, 301°C to 415°C, 165°C to 294°C, and 142°C to 283°C, respectively (Figure 11(d)). The salinity ranged from 13 to 23 wt.% NaCl$_{eq}$, 19 to 23 wt.% NaCl$_{eq}$, 2 to 11 wt.% NaCl$_{eq}$, 1 to 8 wt.% NaCl$_{eq}$, and 1 to 4 wt.% NaCl$_{eq}$, respectively (Figure 10(d)). The density ranged from 0.65 to 1.0 g/cm^{-3}, 0.60 to 1.05 g/cm^{-3}, 0.6 to 0.85 g/cm^{-3}, 0.75 to 0.95 g/cm^{-3}, and 0.75 to 0.95 g/cm^{-3}, respectively (Figure 12(d)). The trapping pressures were esti-mated to range around 180 to 500 bars, 190 to 500 bars, 80 to 200 bars, 8 to 90 bars, and 7 to 70 bars, respectively

(Figure 13(d)). The results show that homogeneous temperature (T_h), salinity, and trapping pressure have obviously decreased from garnet→pyroxene→quartz/I→quartz/II→calcite.

4.1.2. Laser Raman Spectroscopy. For the individual large fluid inclusions with clearly defined boundaries that devel-oped in quartz, Laser Raman analysis revealed that both the liquid-phase and the gas-phase inclusions are composed of H$_2$O (Figure 14).

4.2. Hydrogen and Oxygen Isotope Compositions. The quartz crystals were separated from four samples of MGP and the

(a)

(b)

(c)

(d)
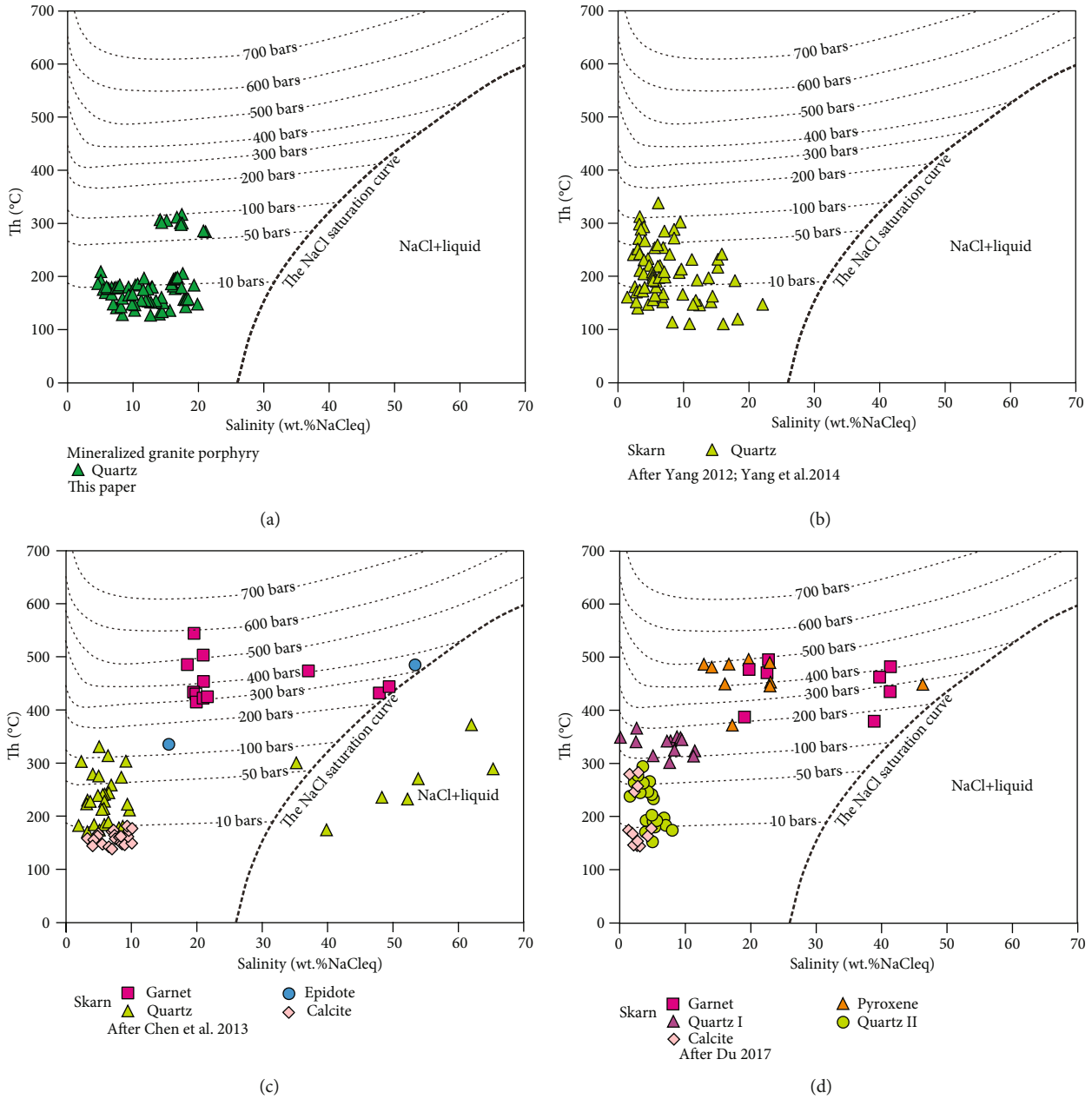
Figure 13: The trapping pressure estimates for fluid inclusions of the MGP (a) and SOB (b–d), YCD, Yunnan, China (after [24, 41–43]).

H isotopic of quartz inclusions and the O isotopic compositions of the quartz were determined. The corresponding $\delta^{18}O_{H2O}$ was calculated using $1000 \ln \alpha_{quartz-water} = 3.42*$ $10^6/T^2 - 2.86$ [48]. For quartz contained in the MGP, $\delta^{18}O_{H2O}$ varied from -1.91‰ to -1.02‰ and averaged at -1.28‰. The δD_{SMOW} ranged from -143.10‰ to -110‰ and averaged at -128.45‰. For quartz from SOB, Zhao [30], Chen et al. [27], and Yang et al. [26] had reported the $\delta^{18}O_{H2O}$ values ranging from -3.05‰ to 4.85‰ ($n = 17$) and averaging around 1.61‰. The δD_{SMOW} varied from -120‰ to -76.2‰ ($n = 17$), averaging at -96.49‰ (Table 3). Du [24] had reported the $\delta^{18}O_{H2O}$ values ranging from 3.9‰ to 8.6‰, and the δD_{SMOW} varied from -119.3‰ to -107.8‰ ($n = 9$) in garnet of SOB (Table 3).

4.3. Sulfur Isotopic Compositions. The sulfur isotope ratio of pyrite and chalcopyrite separated from the MGP was analyzed (Table 4). In pyrite, the $\delta^{34}S_{V-CDT}$ values ranged from -6.10‰ to 0.80‰ with an average of -1.74‰. In chalcopyrite, the $\delta^{34}S_{V-CDT}$ varied from 0.10‰ to 0.50‰, with an average of -0.70‰. and total sulfur $\delta^{34}S_{\Sigma S} = 0.34$ by calculation. Zhan et al. [2] reported that pyrite and chalcopyrite $\delta^{34}S_{V-CDT}$ values ranged from -1.61‰ to 2.46‰ ($n = 5$) and $\delta^{34}S_{V-CDT}$ values ranged from -3.15‰ to 0.97‰ ($n = 5$), respectively. Pan et al. [31] reported the pyrite and chalcopyrite $\delta^{34}S_{V-CDT}$ values ranged from -2.21‰ to 1.82‰ ($n = 8$) and $\delta^{34}S_{V-CDT}$ values ranged from -3.14‰ to 0.94‰ ($n = 4$), respectively. Zhu [32] reported that pyrite and chalcopyrite $\delta^{34}S_{V-CDT}$ values

(a)

(b)
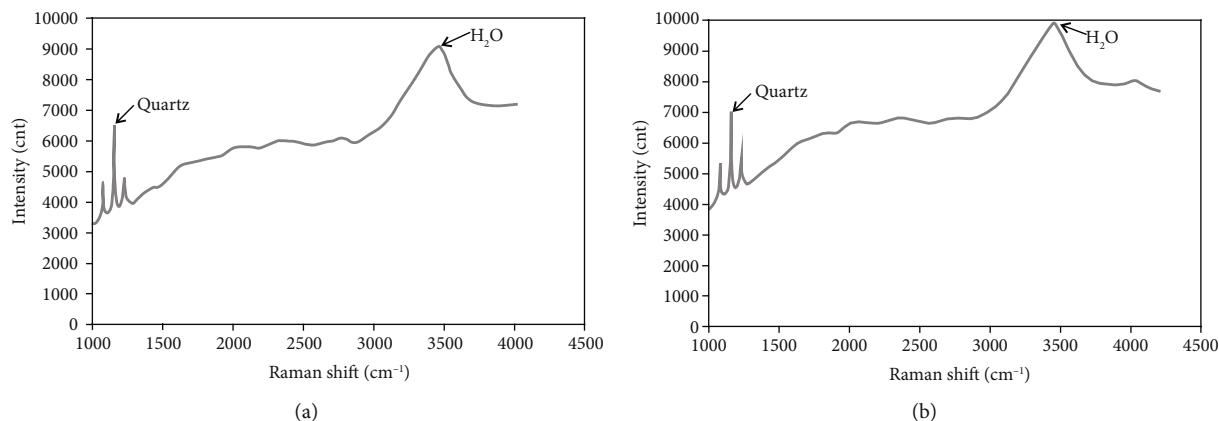
FIGURE 14: Laser Raman spectra for liquid phase (a) and vapor phase (b) of the fluid inclusions in the MGP, YCD, Yunnan, China.

ranged from -1.90‰ to 1‰ ($n = 4$) and $\delta^{34}S_{V-CDT}$ values ranged from -2.60‰ to 1.20‰ ($n = 3$), respectively. Yang et al. [11, 12] reported that the chalcopyrite $\delta^{34}S_{V-CDT}$ values ranged from -4.20‰ to -2.70‰ ($n = 2$). Zhu [19] reported that the molybdenite $\delta^{34}S_{V-CDT}$ values ranged from 0.50‰ to 0.90‰ ($n = 7$) with an average of 0.69‰ and with a difference 0.40‰. Yang et al. [26] reported that pyrite and chalcopyrite $\delta^{34}S_{V-CDT}$ values ranged from -1.0‰ to 0.90‰ ($n = 2$) and $\delta^{34}S_{V-CDT} = -1.60$ ($n = 1$), respectively. Du [24] reported about the pyrite, chalcopyrite, galena, sphalerite, and pyrrhotite, which have $\delta^{34}S_{V-CDT}$ values ranging from -1.97‰ to 2.61‰ ($n = 14$), -2.60‰ to 1.20‰ ($n = 9$), 0.80‰ to 2.11‰ ($n = 5$), 1.10‰ to 1.70‰ ($n = 3$), and -2.60‰ to 0.70‰ ($n = 24$), respectively.

4.4. Pb Isotopic Compositions. The lead isotopic composition of pyrite and chalcopyrite from the MGP and the SOB was also assessed (Table 5). In the MGP, the $^{208}Pb/^{204}Pb$ ranged from 38.8208 to 38.9969 (average of 38.9127), the $^{207}Pb/^{204}Pb$ ranged from 15.7079 to 15.7357 (average 15.7215), and the $^{206}Pb/^{204}Pb$ ranged from 18.5363 to 18.7045 (average 18.6438). The characteristic parameters were $\mu = 9.66 \sim 9.69$, $\omega = 38.14 \sim 38.70$, and Th/U = 3.46 to 3.87. For the SOB, Pan et al. [31], Zhu [32], Yang et al. [11, 12], Zhao [30], and Chen [28] reported that the $^{208}Pb/^{204}Pb$ ranged from 37.8330 to 38.7920 (average 38.49), the $^{207}Pb/^{204}Pb$ ranged from 15.4340 to 15.7230 (average 15.63), and the $^{206}Pb/^{204}Pb$ ranged from 17.9850 to 18.3950 (average 18.28). The characteristic parameters for the skarn ore bodies were $\mu = 9.18$ to 9.70, $\omega = 34.61$ to 39.39, and Th/U = 3.65 to 3.91. The lead isotopic ratio of sulfides in the MGP were lower and more uniform than that of sulfides in SOB.

5. Discussion

5.1. Source of Original Ore-Forming Fluids. For quartz contained in the MGP relation to meteoric water ($\delta D = -350‰$ to +50‰, $\delta^{18}O_{H2O} = -44‰$ to +10‰) and magmatic water ($\delta D = -50‰$ to -80‰, $\delta^{18}O_{H2O} = 7.0‰-9.5‰$), the δD-$\delta^{18}O_{H2O}$ diagram of H-O isotopes in quartz was located within the ranges between the meteoric water and the

magmatic water area (Figure 15). δD_{Quartz} (-143.10‰ to -110‰) in MGP < $\delta D_{Garnet-Quartz}$ (-120‰ to -76.2‰) in SOB; $\delta^{18}O_{H2O(Quartz)}$ (-1.91‰ to -1.02‰) in MGP < $\delta^{18}O_{H2O(Garnet-Quartz)}$ (-3.05‰ to 8.60‰) in SOB. Both the δD-$\delta^{18}O_{H2O}$ diagrams indicate the presence of magmatic and meteoric water. However, the SOB were generally closer to the magmatic water, and it may show an evolutionary trend away from magmatic water (Figure 15(b)). Meanwhile, the MGP was located in the region between the meteoric water and the magmatic water, and its δD and $\delta^{18}O_{H2O}$ values were lower than those of the SOB (garnet-quartz). This maybe because the carbonate replacement formed by SOB was a high-temperature magmatic hydrothermal fluid, at this moment, allowing only a few of meteoric water to infiltrate ore-forming fluid, resulting in the δD-$\delta^{18}O_{H2O}$ diagram appearing closer to the magmatic water. Along the continuous evolution of ore-forming fluid, the amount of infiltrating meteoric water increased, forming low-temperature ore-forming fluid, and which may make the metallogenic temperature decrease (the homogenization temperatures of fluid inclusions have decreased), which will make the δD and $\delta^{18}O_{H2O}$ values decrease. Finally, the δD and $\delta^{18}O_{H2O}$ values show a trend line away from magmatic water or near meteoric water from SOB to MGP (Figure 15(b)), and we believe that the ore-forming fluid originated from the mixture of magmatic water and meteoric water. According the Re-Os age of molybdenite in SOB (228-235 Ma) and the evolution trend of ore-forming fluid, SOB were formed during the early-stage metasomatic interaction with carbonates [15, 16, 34, 49], while porphyry ore bodies were formed during the late stage. The geological evidence are as follows: (i) the ore-forming fluid shows the evolution trend of high temperature-high salinity-high capture pressure to low temperature-low salinity-low capture pressure from SOB to porphyry ore bodies (MGP),and there is an overlap region; (ii) the hydrogen and oxygen isotope composition shows that the SOB→porphyry ore bodies (MGP) have a tendency to be close to meteoric water. It is speculated that the mixing amount of meteoric water gradually increased and finally formed porphyry ore-bodies along with the evolution of ore-forming fluid. Therefore, the skarn and porphyry

TABLE 3: Hydrogen and oxygen isotope compositions of quartz in MGP and SOB, Yangla copper deposit, Yunnan, China.

Sample no.	Location	Minerals	Homogenization temperature (°C)	$\delta^{18}O_{SMOW}$ ‰	δD_{SMOW} ‰	$\delta^{18}O_{H2O}$ ‰	Reference
41-1			182	10.93	-130	-1.91	
41-2	MGP in Linong ore block	Quartz	175	11.57	-143.10	-1.07	
41-3			173	11.65	-110	-1.13	
3250-41-5			171	11.91	-130.70	-1.02	This paper
Totality characteristics			171~182	10.93~11.91	-143.10~-110	-1.91~-1.02	
3175-d8-1			238	11.6	-100	2.06	
3175-d8-2		Quartz	238	11.1	-89	1.56	
3175-d10			238	11.7	-94	2.16	
YL-8			—	—	-100	2.50	
YL-24			—	—	-105	1.16	
YL-39		Quartz	—	—	-104	1.82	[26]
YL-40			—	—	-115	1.54	
YL-41			—	—	-109	0.71	
YL-57	SOB in Linong ore block		—	—	-120	-3.05	
YL3275-27			184	11.1	-89	-2.42	
YL3275-07			250	12.3	-95	2.66	
YL3275-05		Quartz	259	11.8	-89	2.58	[27]
YL3275-26			239	12.2	-88	2.01	
YL3275-28			240	12.5	-112	2.36	
YL3275-21			343	11.0	-77	4.85	
L-2		Quartz	250	11.1	-78.1	2.15	[30]
L-6			250	11.6	-76.2	2.65	
Totality characteristics			184~343	11.0~12.5	-120~76.20	-3.05~4.85	
Totality characteristics		Garnet	—	—	-119.3~-107.8	3.90~8.60	[24]

ore bodies were maybe the products of continuous evolution in the same magmatic fluid system and formed in different stages.

The determination of sulfur element sources in deposits must be based on the total sulfur isotopic composition ($\delta^{34}S_{\Sigma S}$) in the ore-forming hydrothermal fluid during sulfide precipitation. Experimental studies show (Zheng et al. 2000) that the hydrothermal system ^{34}S order is $SO_4^{2-} > HSO_4^- > SO_2^{2-} > SO_2 > S_x > H_2S > HS > S^{2-}$ under the condition of isotope exchange equilibrium. Therefore, based on the theory of equilibrium crystallization of sulfur isotopes in solution, when sulfur isotopic fractionation reaches equilibrium conditions, the sequence of the enriched $\delta^{34}S$ is as follows: $\delta^{34}S_{sulfate} \gg \delta^{34}S_{molybdenite} > \delta^{34}S_{pyrite} > \delta^{34}S_{sphalerite} > \delta^{34}S_{pyrrhotite} > \delta^{34}S_{chalcopyrite} > \delta^{34}S_{galena} > \delta^{34}S_{chalcocite} > \delta^{34}S_{argentite} > \delta^{34}S_{cinnabar}$, when sulfur fractionation reaches equilibrium conditions, the pyrite and pyrrhotite $\delta^{34}S$ values can represent the total sulfur ($\delta^{34}S_{\Sigma S}$) in the ore-forming fluid [50, 51]. Out of the 5 tested samples, only the YS-3 sample exhibited $\delta^{34}S_{pyrite} > \delta^{34}S_{chalcopyrite}$, with the sulfur fractionation process reaching equilibrium conditions, while the remaining 4 samples exhibited $\delta^{34}S_{chalcopyrite} > \delta^{34}S_{pyrite}$, with the sulfur fractionation not reaching equilibrium conditions. But, the $\delta^{34}S$ has a sequence of mineral enrichment for most

sulfide samples in the YCD, pyrite>sphalerite>pyrrhotite>chalcopyrite>galena ([24]). Such as the samples LN-62, YK003,YK015-2, LN81, YK007-1, and YK017-3, pyrite (−1.97) > pyrrhotite (−2.48), pyrite (−0.80) > pyrrhotite (−0.98), pyrite (2.00) > galena (−0.78), pyrrhotite (0.08) > chalcopyrite (−0.69), pyrite (2.61) > sphalerite (1.55) > galena (−0.18), and sphalerite (1.70) > pyrrhotite (0.74) > galena (0.31), respectively (Table 4). Based on the $\delta^{34}S$ sequence of minerals enrichment for most sulfide samples in this deposit (the sample YS-3 and most of the SOB sulfide samples), we concluded that the hydrogen sulfide (H_2S) in the ore-forming system during the ore-forming period practically reached equilibrium [19, 24]. Therefore, the total sulfur isotopic composition ($\delta^{34}S_{\Sigma S}$) can be determined using the following two methods.

5.1.1. Sulfur-Bearing Mineral Assemblage Estimated $\delta^{34}S_{\Sigma S}$. Sulfide compounds in the Linong ore block of the YCD have simple compositions and do not contain sulfate minerals. They are mainly composed of pyrrhotite, pyrite, chalcopyrite, molybdenite, and sphalerite. Its main soluble form is H_2S, which is a reductive fluid with pH > 6 [28]. The average value of sulfide $\delta^{34}S$, especially the pyrite $\delta^{34}S$ value, can approximately represent the total sulfur $\delta^{34}S_{\Sigma S}$ [51] in the hydrothermal fluid. In addition, the sulfur isotope value is a function of

TABLE 4: S isotopic compositions for sulfide mineral pair and equilibrium states of the MGP and part SOB in Yangla copper deposit, Yunnan, China.

Sample no.	Minerals	Location	$\delta^{34}S_{V\text{-}CDT}$/‰	$\delta^{34}S$	Equilibrium states	Reference
YS-2	Pyrite		-6.10	Pyrite < chalcopyrite	Nonequilibrium	
	Chalcopyrite		0.20			
YS-3	Pyrite		0.80	Pyrite > chalcopyrite	Equilibrium	
	Chalcopyrite		0.10			
YS-7	Pyrite	MGP in Linong ore block	-0.30	Pyrite < chalcopyrite	Nonequilibrium	This paper
	Chalcopyrite		0.50			
YS-9	Pyrite		-2.60	Pyrite < chalcopyrite	Nonequilibrium	
	Chalcopyrite		0.50			
YS-10	Pyrite		-0.50	Pyrite < chalcopyrite	Nonequilibrium	
	Chalcopyrite		0.40			
Totality characteristics				Range -6.10~0.80, average -0.70, difference 6.90, $\delta^{34}S_{\Sigma S} = 0.34$		
LN-62	Pyrite		-1.97	Pyrite > chalcopyrite	Equilibrium	
	Chalcopyrite		-2.48			
LN-68	Pyrite		-1.72	Pyrite > pyrrhotite	Equilibrium	
	Pyrrhotite		-1.82			
LN-74	Pyrite		0.66	Pyrite > chalcopyrite	Equilibrium	
	Chalcopyrite		-1.94			
LN-75	Chalcopyrite		-1.76	Chalcopyrite > pyrrhotite	Nonequilibrium	
	Pyrrhotite		-1.93			
YK003	Pyrite		-0.80	Pyrite > pyrrhotite	Equilibrium	
	Pyrrhotite		-0.98			
YK004-1	Pyrite		-0.85	Pyrite > pyrrhotite	Equilibrium	
	Pyrrhotite		-0.91			
YK007-1	Pyrite		2.61	Pyrite > galena > sphalerite	Equilibrium	
	Galena		-0.18			
	Sphalerite		1.55			
YK015-1	Pyrite		0.34	Pyrite > chalcopyrite	Equilibrium	
	Chalcopyrite		-1.07			
YK015-2	Pyrite	SOB in Linong ore block	2.00	Pyrite > galena	Equilibrium	[24]
	Galena		-0.78			
YK017-3	Pyrrhotite		0.74	Sphalerite > pyrrhotite > galena	Equilibrium	
	Galena		0.31			
	Sphalerite		1.70			
L33	Pyrite		1.20	Pyrite > chalcopyrite	Equilibrium	
	Chalcopyrite		0.97			
L81	Pyrrhotite		0.08	Pyrrhotite > chalcopyrite	Equilibrium	
	Chalcopyrite		-0.69			
L203	Pyrrhotite		-0.42	Pyrite > pyrrhotite	Equilibrium	
	Pyrite		0.12			
S1	Pyrite		-1.90	Pyrite = pyrrhotite	Nonequilibrium	
	Pyrrhotite		-1.90			
S2	Pyrite		-1.00	Pyrite < chalcopyrite	Nonequilibrium	
	Chalcopyrite		-0.80			
S3	Pyrite		1.00	Chalcopyrit > pyrite > galena	Nonequilibrium	
	Galena		0.30			
	Chalcopyrite		1.20			
S5	Pyrite		-1.90	Pyrite > chalcopyrite	Equilibrium	
	Chalcopyrite		-2.60			
Totality characteristics				Range -2.60~2.61, average -0.42, difference 5.21		

TABLE 5: Pb isotopic compositions of the MGP and SOB in Yangla copper deposit, Yunnan, China.

Sample no.	Location	Minerals	$^{206}Pb/^{204}Pb$	$^{207}Pb/^{204}Pb$	$^{208}Pb/^{204}Pb$	$^{206}Pb/^{207}Pb$	t (Ma)	μ	ω	Th/U	V1	V2	$\Delta\alpha$	$\Delta\beta$	$\Delta\gamma$	Reference
YS-1			18.6945	15.7302	38.9698	1.1884	124	9.69	38.35	3.83	78.92	63.30	86.63	26.35	45.40	
YS-4			18.6548	15.7145	38.9023	1.1871	133	9.66	38.14	3.82	76.95	62.19	85.02	25.36	43.98	
YS-5			18.5363	15.7079	38.8208	1.1801	209	9.66	38.41	3.85	77.63	60.92	84.14	25.27	45.18	
YS-5		Pyrite	18.5876	15.7211	38.8907	1.1823	189	9.68	38.53	3.85	79.11	61.95	85.51	26.04	46.15	
YS-6			18.6774	15.726	38.9256	1.1877	131	9.68	38.22	3.82	77.95	63.21	86.19	26.11	44.52	
YS-8			18.5567	15.7165	38.9	1.1807	205	9.68	38.70	3.87	79.76	61.04	85.00	25.81	47.13	
3250-41lb2	MGP in Linong ore block		18.6577	15.7241	38.9373	1.1866	142	9.68	38.36	3.84	78.59	62.64	85.95	26.03	45.35	This paper
YS-1			18.6928	15.7231	38.9426	1.1889	116	9.68	38.18	3.82	77.67	62.99	85.94	25.85	44.33	
YS-4			18.8636	15.7357	38.9969	1.1988	8.70	9.68	37.59	3.76	75.50	65.85	87.58	26.25	41.11	
YS-5		Chalcopyrite	18.5403	15.7129	38.8355	1.1799	212.4	9.67	38.49	3.85	78.33	61.23	84.62	25.61	45.71	
YS-6			18.7045	15.7301	38.9591	1.1891	116.2	9.69	38.25	3.82	78.38	63.55	86.64	26.31	44.79	
YS-8			18.564	15.7138	38.8653	1.1814	196.6	9.67	38.49	3.85	78.48	61.30	84.76	25.60	45.82	
3250-41lb1			18.639	15.7238	38.9191	1.1854	155.3	9.68	38.39	3.84	78.63	62.56	85.88	26.07	45.44	
Totality characteristics			$^{208}Pb/^{204}Pb = 38.8208 \sim 38.9969$, $^{207}Pb/^{204}Pb = 15.7079 \sim 15.7357$, $^{206}Pb/^{204}Pb = 18.5363 \sim 18.7045$, $\mu = 9.66 \sim 9.69$, $\omega = 38.14 \sim 38.70$, Th/U = 3.46~3.87													
1			18.277	15.627	38.454	1.1696	296.6	9.53	37.58	3.82	68.60	54.78	75.89	20.41	39.16	
2		Chalcopyrite	18.313	15.672	38.602	1.1685	324.7	9.62	38.42	3.87	75.25	57.37	80.28	23.49	44.42	[32]
3			18.369	15.68	38.611	1.1715	294.5	9.63	38.22	3.84	74.63	58.68	81.14	23.86	43.31	
4			18.316	15.675	38.574	1.1685	326.2	9.62	38.32	3.86	74.76	57.98	80.58	23.69	43.73	
Yn-19			18.249	15.622	38.435	1.1682	310.6	9.53	37.61	3.82	68.46	54.21	75.37	20.15	39.27	
Yn-60			18.30	15.638	38.459	1.1702	293.3	9.55	37.57	3.81	69.07	55.95	76.98	21.11	39.15	
Yn-71		Pyrite	18.221	15.519	38.19	1.1741	204.2	9.32	35.78	3.72	53.89	47.90	65.31	12.92	27.98	
yn56a			18.023	15.436	37.833	1.1676	246.4	9.18	34.61	3.65	43.24	42.31	57.00	7.69	20.19	
yn20			18.256	15.59	38.334	1.1710	266.7	9.46	36.84	3.77	62.90	52.73	72.27	17.84	34.60	[31]
Yn-37			18.112	15.45	37.998	1.1723	197.7	9.20	34.94	3.68	45.97	42.79	58.43	8.39	22.53	
yn47-1	SOB in Linong ore block		18.15	15.506	38.177	1.1705	240.3	9.31	35.99	3.74	54.40	46.03	63.97	12.24	29.20	
yn58		Chalcopyrite	18.205	15.541	38.178	1.1714	243.5	9.37	36.02	3.72	56.08	49.68	67.44	14.54	29.37	
yn65			17.985	15.434	38.358	1.1653	272.3	9.18	36.99	3.90	56.89	35.81	56.79	7.69	35.49	
YL-13			18.326	15.715	38.713	1.1661	366.2	9.70	39.24	3.92	81.45	59.91	84.44	26.51	49.29	
YL-56		Pyrite	18.348	15.703	38.691	1.1684	336.6	9.67	38.90	3.89	79.23	59.43	83.31	25.57	47.36	[11, 12]
YL-50			18.346	15.716	38.721	1.1673	353.3	9.70	39.16	3.91	81.18	60.16	84.56	26.51	48.92	
YL-53		Chalcopyrite	18.346	15.711	38.72	1.1677	347.4	9.69	39.11	3.91	80.70	59.75	84.08	26.15	48.63	
LN-2			18.323	15.682	38.616	1.1684	329.5	9.64	38.52	3.87	76.21	58.19	81.26	24.16	45.01	
LN-3		Chalcopyrite	18.343	15.681	38.622	1.1698	314.2	9.63	38.42	3.86	75.72	58.30	81.20	24.02	44.49	[30]
LN-4			18.321	15.651	38.641	1.1706	294	9.57	38.34	3.88	74.08	55.28	78.27	21.96	44.10	

TABLE 5: Continued.

Sample no.	Location	Minerals	^{206}Pb/^{204}Pb	^{207}Pb/^{204}Pb	^{208}Pb/^{204}Pb	^{206}Pb/^{207}Pb	t (Ma)	μ	ω	Th/U	V1	V2	$\Delta\alpha$	$\Delta\beta$	$\Delta\gamma$	Reference
YLV-04		Pyrite	18.395	15.683	38.63	1.1729	279.6	9.63	38.18	3.84	74.64	59.06	81.47	23.98	43.16	
			18.37	15.723	38.792	1.1684	344.7	9.71	39.39	3.93	82.87	60.27	85.27	26.92	50.46	[28]
YLT K-12	Jun-75	Chalcopyrite	18.359	15.706	38.726	1.1689	332.4	9.68	39.01	3.90	80.04	59.44	83.62	25.75	48.12	
3275-24			18.362	15.718	38.767	1.1682	344.4	9.70	39.28	3.92	82.03	60.02	84.78	26.59	49.77	
Totality characteristics		^{208}Pb/^{204}Pb = 37.8330~38.7920, ^{207}Pb/^{204}Pb = 15.4340~15.7230, ^{206}Pb/^{204}Pb = 17.9850~18.3950, μ = 9.18~9.70, ω = 34.61~39.39, Th/U = 3.65~3.91														
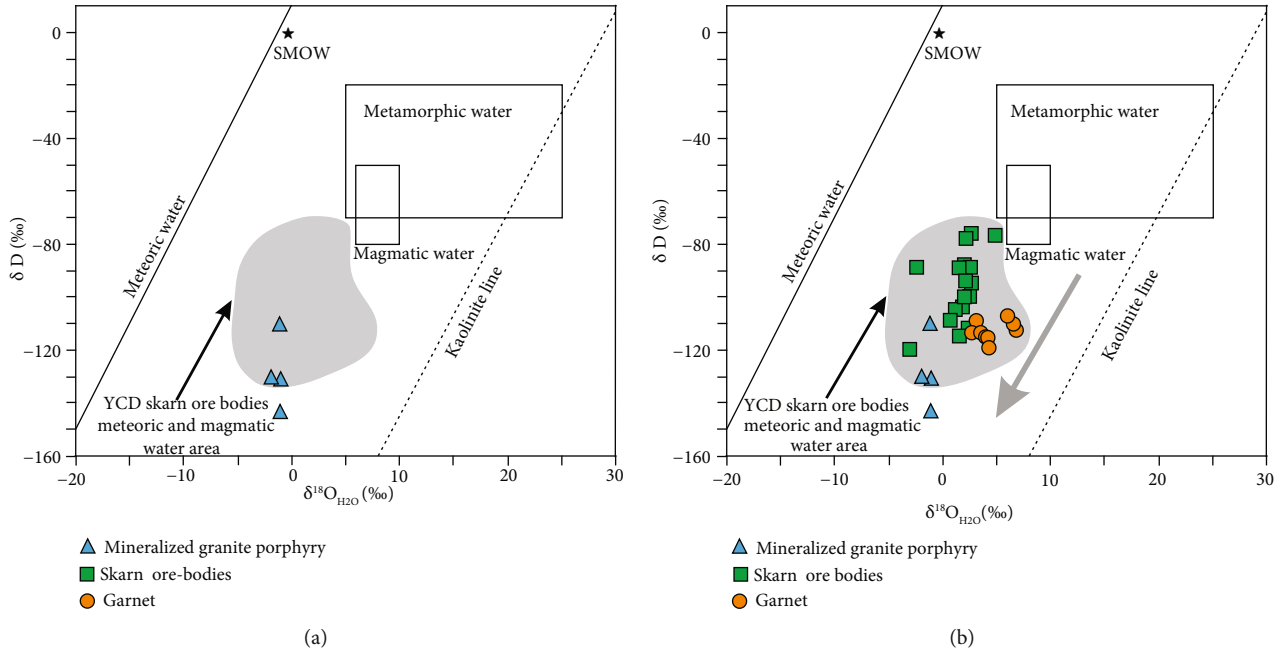
Figure 15: δD-$\delta^{18}O_{H_2O}$ diagram of the quartz in the MGP (a) and SOB (b), YCD, Yunnan Province, China.

pH, temperature, Eh and oxygen fugacity, and it is influenced significantly by physical and chemical conditions [52]. It is possible that the varying chemical and physical conditions during different stages of mineralization and superimposed mineralization may have led to nonequilibrium fractionation of sulfur isotopes in sulfides. This conclusion is consistent with the composite formation of the ore deposit. In the MGP of the YCD, the sulfide $\delta^{34}S_{V\text{-CDT}}$ variation range being concentrated between -1.0‰ and 1.0‰, the pyrite $\delta^{34}S_{V\text{-CDT}}$ values were concentrated between 1 and -7‰, and the chalcopyrite $\delta^{34}S_{V\text{-CDT}}$ values were concentrated between 1 and 0‰ (Figure 16(a)). This is consistent with the research results on the sulfur isotopic composition of sulfides in SOB (the $\delta^{34}S_{V\text{-CDT}}$ values range from -5‰ to 3‰, with an average of -0.30‰ and a difference of 8‰; where the pyrite $\delta^{34}S_{V\text{-CDT}}$ values range from -3‰ to 3‰, with an average of -0.50‰ and a difference of 6‰; the chalcopyrite $\delta^{34}S_{V\text{-CDT}}$ values range from -5‰ to 3‰, with an average of -1‰ and a difference of 8‰; the pyrrhotite $\delta^{34}S_{V\text{-CDT}}$ values range from -3‰ to 1‰, with an average of -1.25‰ and a difference of 4‰; the galena $\delta^{34}S_{V\text{-CDT}}$ values range of -1‰ to 3‰, with an average of 0.34‰ and a difference of 4‰; the sphalerite $\delta^{34}S_{V\text{-CDT}}$ values range from 1‰ to 2‰, with an average of 1.43‰ and a difference of 1‰; the molybdenite $\delta^{34}S_{V\text{-CDT}}$ values range from 0‰ to 1‰, with an average of 0.69‰ and a difference of 1‰; the chalcocite $\delta^{34}S_{V\text{-CDT}}$ values range from 1‰ to 2‰, with an average of 1.50‰ and a difference of 1‰) (Tables 4 and 6, Figure 16(b)). The total sulfur isotopic composition was close to -1‰ to 1‰, while its total homogenization was high and the variation range was small. Moreover, it had a single source of sulfur. All of these characteristics point to deep crust or mantle sulfur, indicating that the sulfur source of the MGP and the SOB was the same, originating

in the deep crust-mantle magma. Moreover, the sulfur source was relatively solitary and without contamination by upper crust sediments.

5.1.2. Isotope Diagram Method Estimation of $\delta^{34}S_{\Sigma S}$. This method, also known as the Pinckney method [53], is based on the assumption that when ore-forming fluid isotopes reach equilibrium, the sulfur isotopic composition of the mineral can be considered a function of the temperature and the total sulfur isotopic composition of the ore-forming fluid, that is $1000 \ln \alpha_{x-y} = A^* 10^6/T^2 + B$, where $1000 \ln \alpha = \delta^{34}S_{mineral\ 1} - \delta^{34}S_{mineral\ 2}$, $B = 0$. It is evident that at high temperatures, the $\delta^{34}S$ values of each sulfide in the ore-forming fluid are close to the $\delta^{34}S_{\Sigma S}$ values. If more than two minerals are crystallized from chemically and isotopically homogeneous ore-forming fluid with varying temperature, the sample should approximate a straight line on the $1000\ln\alpha_{x-y}$ versus the $\delta^{34}S_x$ and $\delta^{34}S_y$ diagram. The $\delta^{34}S$-axis intercept is the $\delta^{34}S_{\Sigma S}$ values of the ore-forming fluid. Through interpolation, we determined the pyrite-chalcopyrite (belonging to the one ore-forming fluid) content in the MGP to be $\delta^{34}S_{\Sigma S\ pyrite\text{--}chalcopyrite} = 0.34‰$ (Figure 17(a)) and calculated the sulfides of the $\delta^{34}S_{\Sigma S\ pyrite\text{--}pyrrhotite} = -1.22‰$, $\delta^{34}S_{\Sigma S\ pyrite\text{--}chalcopyrite} = -0.40‰$, $\delta^{34}S_{\Sigma S\ pyrite\text{--}Galena} = 0.56‰$, $\delta^{34}S_{\Sigma S\ pyrrhotite\text{--}chalcopyrite} = -1.57‰$, and $\delta^{34}S_{\Sigma S\ Galena\text{--}Sphalerite} = 2.31‰$ in SOB (Figures 17(b)–17(f)). The values approached -1‰ to 1‰, which is consistent with the characteristics of deep-crust or mantle magma sulfur. This indicates that the sulfur source of the MGP originated in the deep crust-mantle magma, which are consistent with the $\delta^{34}S$ values (-2‰ to 2‰) of SOB sulfides and sulfur-containing mineral assemblage estimation results of $\delta^{34}S_{\Sigma S}$.
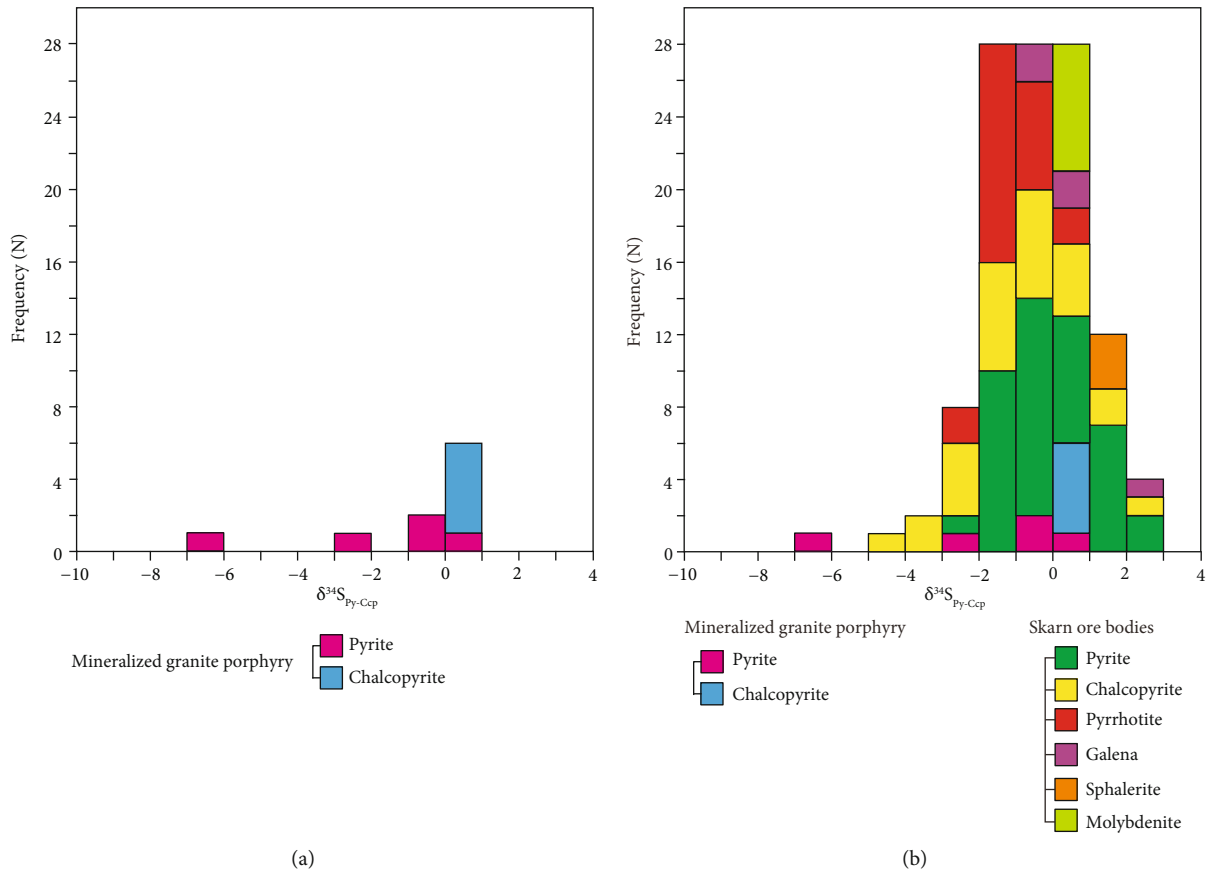
FIGURE 16: S isotopic distribution patterns of the pyrite and chalcopyrite in MGP (a) and SOB (b), YCD, Yunnan, China.

After plotting the lead isotopic composition on a $^{207}Pb/^{204}Pb$-$^{206}Pb/^{204}Pb$ and $^{208}Pb/^{204}Pb$-$^{206}/^{204}Pb$ diagram [54], which reflects the tectonic setting of the lead source region, and the lead isotope data fell close to the upper crust evolutionary line on the $^{207}Pb/^{204}Pb$-$^{206}Pb/^{204}Pb$ diagram (Figure 18(a)) and between the orogenic zone and the lower crust evolutionary lines on the $^{208}Pb/^{204}Pb$-$^{206}/^{204}Pb$ diagram, being closer to the former (Figure 18(b)). This is consistent with the geological background of the Jinshajiang ocean basin westward subduction and collisional orogenic with Changdu-Simao block, indicating that the lead source was the upper crust. The lead isotope relative variogram $\Delta\gamma - \Delta\beta$ is projected onto the $\Delta\gamma - \Delta\beta$ genetic classification diagram [55] (Figure 19(a)). The lead isotope composition mainly falls within the range of upper crust lead, which is dominantly consistent with the distribution of the lead source on the tectonic evolution diagram (Figure 17).

These results are not consistent with the research results of the lead isotopic composition in SOB ($^{208}Pb/^{204}Pb = 37.8330$-$38.7920$, $^{207}Pb/^{204}Pb = 15.4340$-$15.7230$, $^{206}Pb/^{204}Pb = 17.9850$-$18.3950$). The Pb isotopic compositions of ore sulfides from SOB show a linear distribution trend of crust-mantle, indicating a crust-mantle mixing source (Figures 18 and 19(b)). But the lead isotopic composition of MGP was more stable and homogeneous than that of SOB, and its evolutionary range was narrower and shows a upper crust source (Figures 17 and 18(a)). The

difference of Pb isotope source region in MGP and SOB may be the gradually blend of upper crust sediments during the mantle magmatic fluid evolution process. According to the results of fluid inclusion, the ore-forming fluids show an evolutionary trend from high temperature-high salinity-high capture pressure to low temperature-low salinity-low capture pressure from skarn metallogenic stage to porphyry metallogenic stage. It means that there may be upper crust sediments added in the evolution process of ore-forming fluid, which makes it present the high to low level evolution trend. So, the evolution process of the magmatic fluid may be as follows: in the early stage of evolution process, the amount of upper crust sediments were less and formed SOB, and the mixing amount of upper crust sediments gradually increased along with the progress of mineralization. In the late stage, the magmatic fluid already have contained a large amount of upper crust sediments, which made the lead mainly derived from the upper crust in MGP phenomenon. Finally, the lead was mainly derived from the crust-mantle and upper crust in the SOB and MGP, respectively.

5.2. Evolution of Ore-Forming Fluid. According to the temperature measurement results of fluid inclusions in garnet, epidote, and pyroxene, they show that the ore-forming fluid of skarn stage has high temperature and high salinity characteristics (Figures 10–12) [24, 25, 27]. Next, the research results of fluid inclusions in quartz indicates that the

TABLE 6: S isotopic compositions of the MGP and SOB in Yangla copper deposit, Yunnan, China.

| Sample no.	Location	Minerals/number	$\delta^{34}S_{V-CDT}$/‰	Reference
YS-2, YS-3, YS-7, YS-9, YS-10	MGP in Linong ore block	Pyrite/5	-6.10, 0.80, -0.30, -2.60, -0.50	This paper
		Chalcopyrite/5	0.20, 0.10, 0.50, 0.50, 0.40	
Totality characteristics			Range -6.10~0.80, average -0.70, difference 6.90	
L33, L184, L203, L266, L280		Pyrite/5	1.20, -0.60, 0.12, 2.46, -1.61	[2]
L33, L81, L128, L135, L57		Chalcopyrite/5	0.97, -0.69, 0.03, -0.82, -3.15	
S_1, S_2, S_3, S_5		Pyrite/4	-1.90, -1.00, 1.00, -1.90	[32]
S_2, S_3, S_5		Chalcopyrite/3	-0.80, 1.20, -2.60	
YL-50, YL-53		Chalcopyrite/2	-4.20, -2.70	[11, 12]
YLV-04, YLTK-12	SOB in Linong ore block	Pyrite/2	-1.00, 0.90	[26]
YL3075-24		Chalcopyrite/1	-1.60	
Yn-126, yn-60, yn-19, yn-47, yn-56a, yn-108, yn-20, yn-29		Pyrite/8	0.27, -0.68, -0.90, 1.82, -0.72, 1.53, -2.21, -0.89	[31]
Yn-37, yn-71, yn-58b, yn-65		Chalcopyrite/4	-1.98, 0.94, -0.90, -3.14	
Y-1-2, Y-3, Y-6, Y-7, Y-8, Y-9		Pyrite/6	1.64, -1.62, -0.17, -0.24, -1.25, -0.91	[30]
Y-4, Y-5		Chalcopyrite/2	2.29, -1.07	
Totality characteristics			Range -4.20~2.46, average -0.59, difference 6.66	
—	SOB in Linong ore block	Molybdenite/7	0.5, 0.6 ,0.7, 0.9, 0.6, 0.7, 0.8	[19]
Totality characteristics			Range 0.50~0.90, average 0.69, difference 0.40	
Totality characteristics		Galena/5	Range 0.80~2.11, average 0.34, difference 2.91	
Totality characteristics	SOB in Linong ore block	Sphalerite/3	Range 1.10~1.70, average 1.43, difference 0.60	[24]
Totality characteristics		Pyrrhotite/24	Range -2.60~0.70, average -1.25, difference 3.30	

coexistence of low temperature medium-to-high salinity and medium temperatur-to-high salinity and the results of fluid inclusions in calcite indicate that ore-forming fluid in the calcite-sulfide stage has the characteristics of low temperature and low salinity (Figure 12) [24, 25, 27]. In short, from the early skarn stage to the late calcite-sulfide stage, the homogenization temperature and salinity of the ore-forming fluid has obviously decreased, and the homogeneous temperature and salinity of the adjacent stages have overlap regions, which show that the ore-forming fluid is continuous evolution [17, 24–27, 29, 32, 56, 57]. As the fluid inclusions developed in quartz of MGP, the homogenization temperatures are mainly concentrated between 120°C-200°C and 280°C-320°C, compared with the previous research results of fluid inclusions developed in quartz of SOB, there are overlap regions (Figures 10–13). Generally speaking, the homogenization temperatures of fluid inclusions from SOB to MGP present a trend from high to low level (420°C-220°C→200°C-120°C), namely, the homogenization temperature of $Th_{MGP} \leq Th_{SOB}$, besides, the salinity of $S_{MGP} \leq S_{SOB}$, the density of $D_{MGP} \leq D_{SOB}$, and the overall trapping pressure of $P_{MGP} < P_{SOB}$ (Figures 10–13). It maybe during the early stage that the magmatic fluid had high temperature, high pressure, high salinity, and low density at this moment, and the magmatic fluid metasomatic interaction with carbonates and formed SOB. Next, as the magmatic fluid continued to evolution, and meteoric water infiltrated, the temperature dropped, followed the suddenly release of pressure caused by fracturing, and hydraulic cracking action, which caused ore-forming fluid trapping pressure and density to decrease. The sedimentary materials of upper crust may contribute to some metallic elements and ore-forming fluid replaced interaction with the early-formed skarn metal minerals, which make the ore-forming fluid salinity and density relatively decreased [25, 27, 28]. Hence, the ore-forming fluid has the feature of low temperature, relatively low pressure, relative low salinity, and low density at the late stage. Therefore, according the results of fluid inclusions in quartz of MGP and garnet, epidote, pyroxene, and quartz in SOB, we believe that the evolution of ore-forming fluid is continuous from SOB to MGP, and there may be products that belong to the same ore-forming fluid system.

5.3. Ore-Forming Mechanism. Several authors shows that the mechanism of minerals precipitation in ore-forming fluid are as follows: (1) water-rock reaction, (2) the variation of temperature or (and) pressure, (3) the mix mechanism of ore-forming fluid, and (4) ore-forming fluid immiscibility or (and) boiling mechanism [24, 25, 27, 28, 40, 44]. The fluid inclusions of SOB indicate that the unisothermal mixing, cooling, and boiling actions were the mechanism for metallic mineral precipitation in the YCD [17, 24–27, 29] (Figure 10).
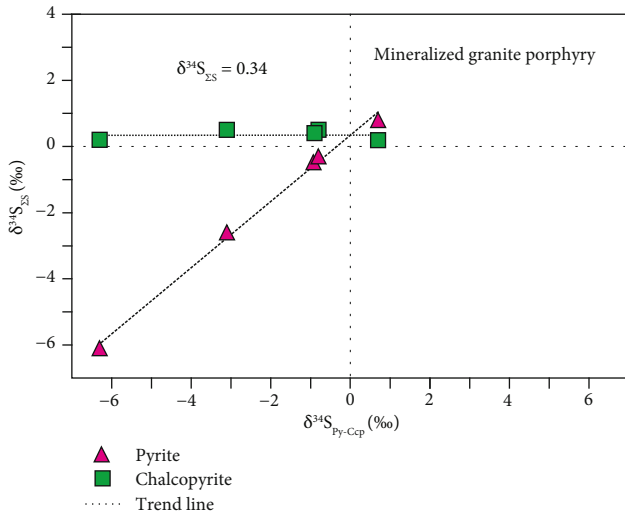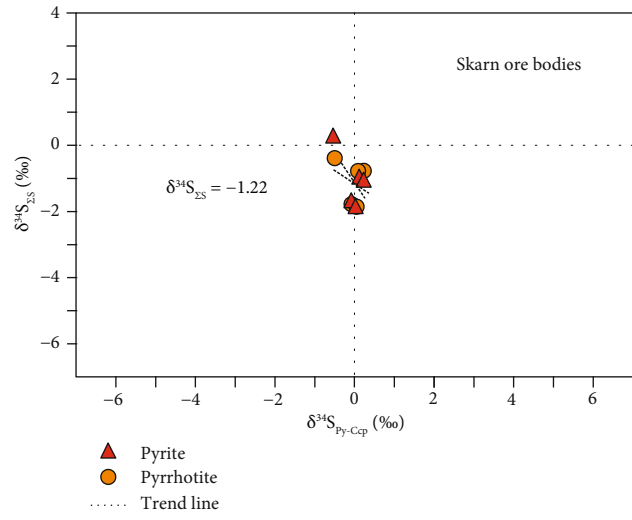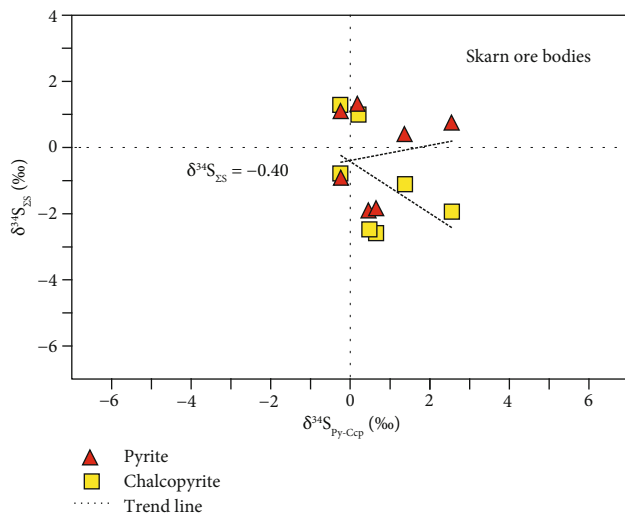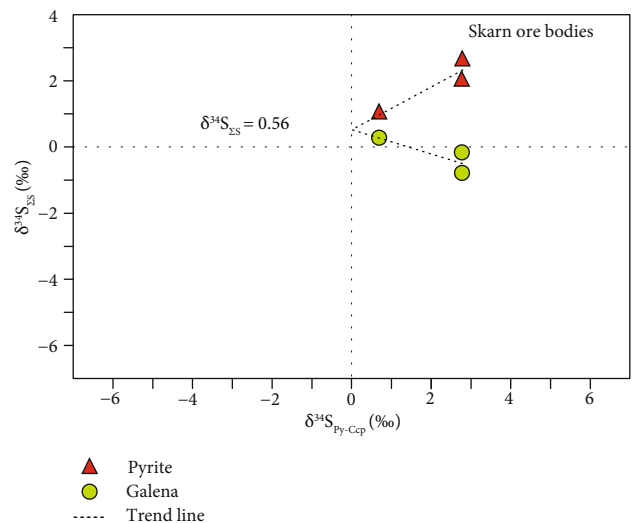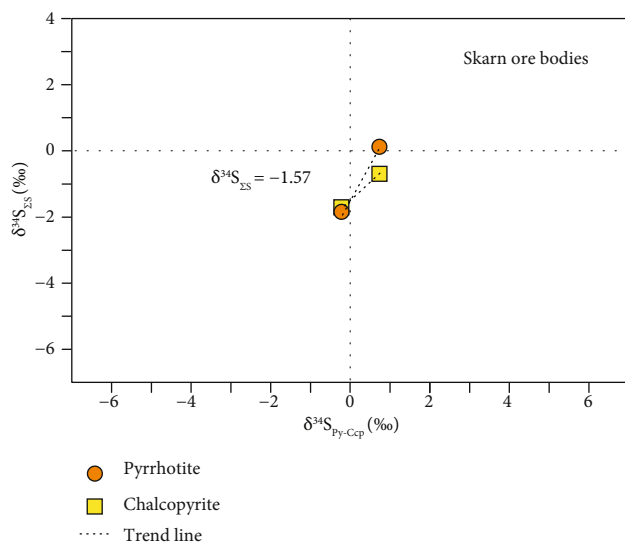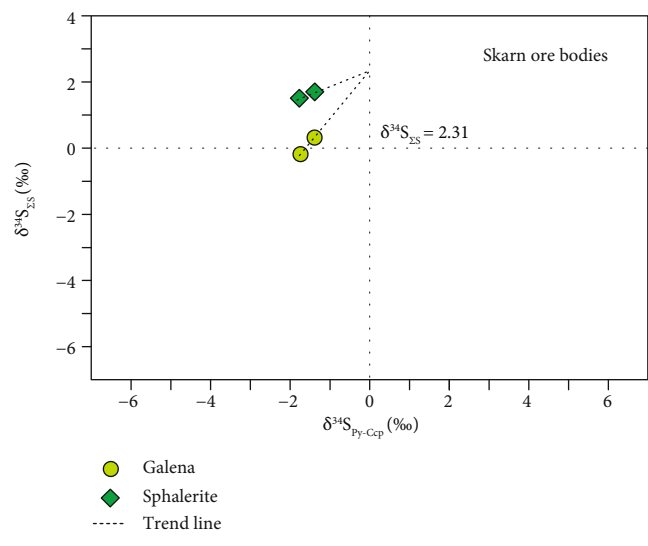
Figure 17: The total sulfur isotopic ($\delta^{34}S_{\Sigma S}$) diagrams of sulfides ($\delta^{34}S_{sulfides}$) in MGP (a) and SOB (b–f), YCD, Yunnan, China.
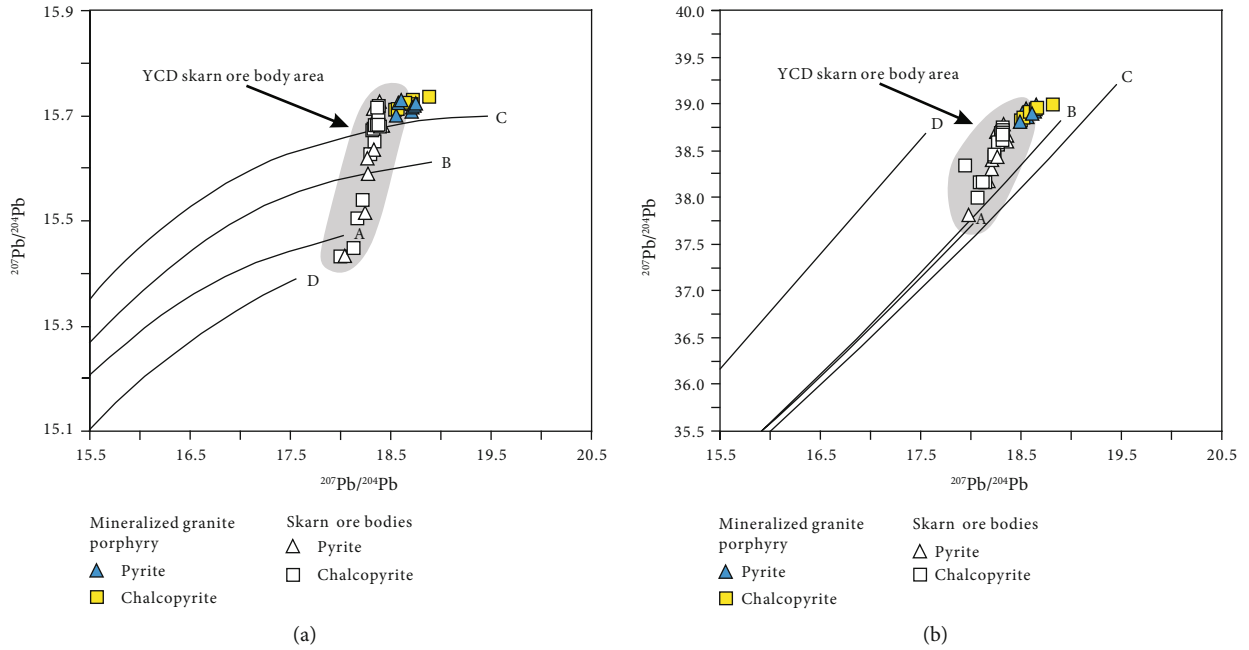
FIGURE 18: Pb isotopic compositions (^{207}Pb/^{204}Pb versus ^{206}Pb/^{204}Pb (a) and ^{208}Pb/^{204}Pb versus ^{206}Pb/^{204}Pb (b)) of the MGP and SOB from the YCD plotted in the model lead evolution diagrams, Yunnan Province, China (after [54]). A-mantle source lead, B-orogenic belt source lead, C-supracrust source lead, D-lower crust source lead.
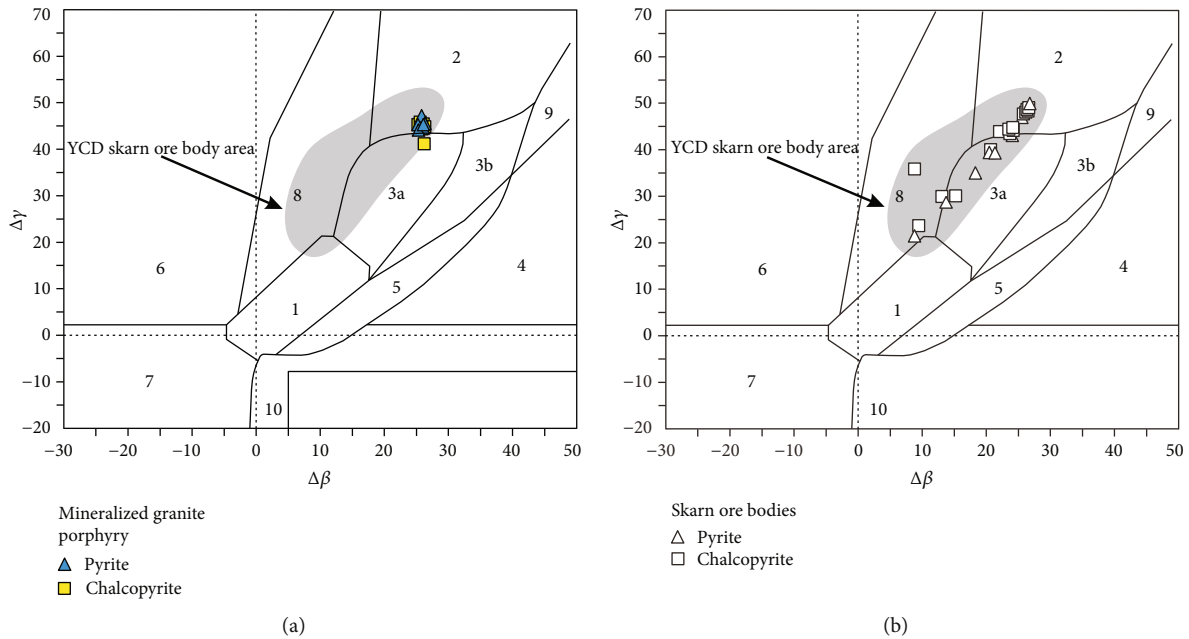
FIGURE 19: $\Delta\gamma$-$\Delta\beta$ diagrams of the Pb isotopes from MGP (a) and SOB (b), YCD, Yunnan, China (after [55]). 1-mantle lead, 2-supracrustal lead, 3-mixed supracrustal and mantle lead (3a-magmatism, 3b-sedimentation), 4-chemical deposit lead, 5-submarine hydrothermal lead, 6-medium-high metamorphic lead, 7-high metamorphic lower crust lead, 8-orogenic belt lead, 9-ancient shales supracrustal lead, and 10-retrograde metamorphic lead. $\Delta\gamma$ and $\Delta\beta$ represent the relative deviation from the same age mantle, $\Delta\beta = [\beta/\beta_{\mathrm{M}}(t) - 1] \times 1000, \Delta\gamma = [\gamma/\gamma_{\mathrm{M}}(t) - 1] \times 1000$, β and γ are the measured values, $\beta_{\mathrm{M}}(t)$ and $\gamma_{\mathrm{M}}(t)$ are the mantle values at t time (t, the ages of the rocks at that periods).

But, in the skarn stage, the ore-forming fluid boiling action may be the main mechanism of metallic mineral precipitation in the YCD [17, 19, 24, 25, 27, 28] and the evidence are as follows: (i) the coexistence phenomenon of gas-liquid phase fluid inclusions, which similar homogeneous temperature and different homogeneous phase states with other types of fluid inclusions are very common under the microscope same field [25, 27, 28]; (ii) there is no obvious variation of

air bubbles after heating up to the homogeneous temperature of some gas-liquid fluid inclusions with medium gas-phase fraction (40%-60%), and it shows that the captured heterogeneous fluid phases are composed of gas and liquid phases in boiling state ([25, 27, 28]; (iii) there are two kinds of primary fluid inclusions (gas-liquid and NaCl-bearing fluid inclusions) with different chemical properties, which have different salinity but similar homogenization temperature, and it shows that they were captured from two different kinds of fluids [25, 27, 28]; (iv) the explosive breccia is developed at the edge and part of the region of the plutons [25, 27, 28]. According to the evolution of ore-forming fluid which is continuous from SOB to MGP and belongs to the products of the same ore-forming fluid system, we believe that in the late stage (porphyritic stage) ore-forming fluid unisothermal mixing and cooling actions may happen (Figure 12). Mineralization process under the unisothermal mixing and cooling actions of medium temperature-medium salinity and low temperature-low salinity ore-forming fluid may exist (Figure 12) [19, 24], and we believe that unisothermal mixing and cooling actions were the main mechanisms at the metallic mineral precipitation in MGP. The unisothermal mixing and cooling actions can cause the dissipation of the volatile components (including CO_2, H_2O, and H_2S), which disrupted the physical and chemical balance of the ore-forming fluid system, causing the precipitation of metallic minerals, such as pyrrhotite, chalcopyrite, pyrite, and bornite [17, 19, 25, 27, 28]. As the temperature and pressure continued to decrease, pyrite, chalcopyrite, bornite, sphalerite, quartz, and calcite were separated in the magmatic fluid [17, 19, 24, 28] and mineralized in the granitic porphyry, meaning that late-stage magmatic fluid formed the porphyritic ore bodies.

5.4. Metallogenic Mechanism of MGP. The Jinshajiang Ocean basin entered a full-scale collisional-orogenic stage in the final stage of the Late Triassic (238-200 Ma) [18, 58–65].The late-stage collision dynamic background caused the upwelling and underplating of the mantle magma, which was closely associated with the mineralization process at the Yangla region [1, 2, 9–12, 16, 25, 27, 30, 49]. The crustal material melted partially forming felsic magma and mixed in the deep magmatic chamber with the mantle-derived magma, forming a mixed parent magma. Then, after undergoing a degree of fractionation, the parent magma formed the granodiorite pluton of the Beiwu, Jiangbian, Linong, and Lunong mining areas. The zircon U-Pb ages of the granodiorite plutons are estimated at 208 Ma-239 Ma (it is mainly concentrated between 227 Ma and 238 Ma) with an average of 230 Ma [15, 16, 18–20, 22], and the Re-Os age of molybdenite in the SOB at 228-235 Ma, average 230 Ma [9–12, 16, 17, 19, 23], which indicates granodiorite pluton and SOB were produced at the same time. Studies have also shown that there is a continuous granitic magma activity in the Yangla region, with a duration of about 15-24 Ma [18], even 33 Ma [66], and combination with the evolution of ore-forming fluid is continuous, and SOB and MGP may be belong to the products of the same ore-forming fluid system. Therefore, we believe that mineralization is continu-
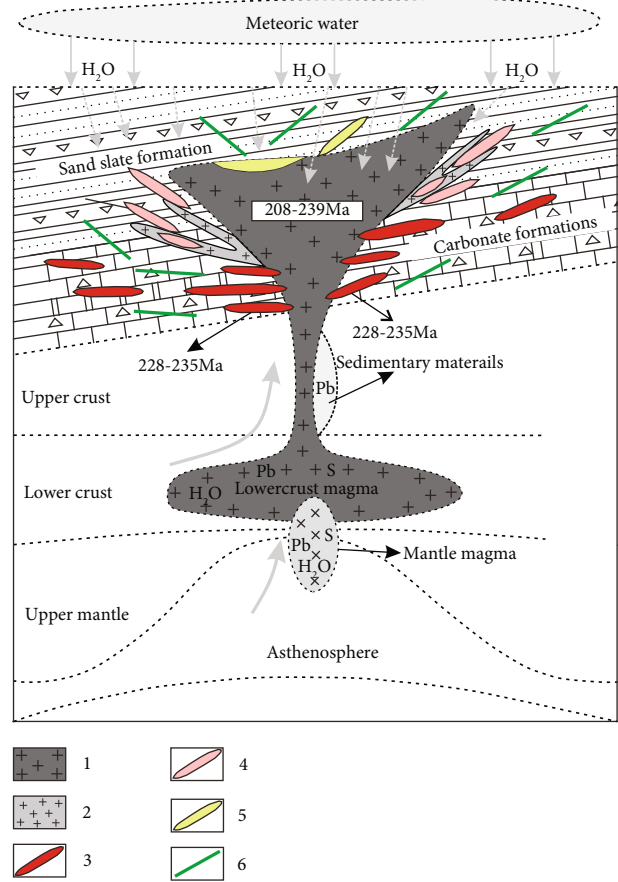
Figure 20: The simple diagram of metallogenic model of the granitic porphyry and granodiorite, YCD, Yunnan, China. 1-granodiorite, 2-granitic porphyry, 3-SOB, 4-porphyry-type ore-bodies, 5-hornfels ore bodies, and 6-veins ore bodies.

ous from SOB (early stage) to MGP (late stage) in the YCD. The S and Pb isotopic components of the MGP reveal that the source of the ore-forming materials was a mixed mantle-crust magmatic fluid, which is in basic accordance with the SOB ore-forming source [16–18, 25, 27, 28, 31, 32, 49]. The H-O isotopic composition of MGP reveals that the source of the ore-forming materials is a mixture of magmatic and meteoric water, which is consistent with the source of SOB [25–27, 29, 30]. The combination of mineralized geology background and the characteristics of fluid inclusions and the H-O, S, and Pb isotopic composition indicates that the metallic minerals in MGP and SOB are products of the same magmatic-meteoric fluid system. Their metallogenic process may have been as follows: in the early stage, high-temperature and high-pressure magma upwelled into the surrounding rock, and after contact metasomatism of carbonates, formed layered and stratified skarn-type and hornfel-type ore bodies in the outer contact zone between the granodiorite pluton and the carbonates; during the late stage, following the continuous crystallization of magma and the persistent meteoric-water infiltration, a mixture of magmatic and meteoric water was formed, followed by the formation of the porphyry-type ore bodies. At the same time, some residual magma migrated along the structural fractures of the

overlying rock formations, and after the infiltration-metasomatism process, it cooled and crystallized forming granite porphyry and the hydrothermal fluids form vein-like ore bodies in granite porphyry (Figure 20).

6. Conclusions

The MGP exhibits dike-type intrusions in the Linong formation, and the overall occurrence have a strike of 60° NE and a steep dip of 40° NW. It is gray and has a porphyritic texture and a massive structure. Its phenocryst components are quartz, plagioclase, and biotite, and its matrix is felsic. A large number of quartz-calcite veins and veinlets, and disseminated pyrite, chalcopyrite, and a small amount of sphalerite have developed in the granitic porphyry pluton, indicating that there is potential for porphyry-type ore bodies in the deep part of the YCD.

The fluid inclusions developed in quartz of MGP indicates that the evolution of ore-forming fluid is continuous from SOB to MGP, and there may belong to the products of the same ore-forming fluid system. There may exist a medium temperature-medium salinity and low temperature-low salinity ore-forming fluid, and the ore-forming fluid unisothermal mixing and cooling actions are may the main mechanism of metallic minerals precipitation in MGP. The H-O isotopic composition shows that the main source of the ore-forming fluid was a gradually evolving mixture of magmatic and meteoric water. The S isotope composition reveals that sulfur originated from the magmatic rocks; the Pb isotope composition showed that the source of lead was the upper crust.

The porphyry-type ore bodies in the granitic porphyry and the skarn-type ore bodies of the YCD most likely belong to the same magmatic fluid system. During the early stage of evolution, the metasomatic interaction of the magmatic fluid and carbonate resulted in forming skarn-type ore bodies, while in the late stage, porphyry-type ore bodies were formed.

Data Availability

The data used to support the findings of this study are available from the corresponding author upon request.

Conflicts of Interest

The authors declare that they have no conflicts of interest.

Acknowledgments

References

[1] G. Q. Yang, *Geological Characteristics, Genisis and Metallogenic Prediction of the Yangla Copper Deposit in Deqin, Yunnan Province, China, [Ph.D. thesis]*, China University of Geosciences, 2009.

[2] M. G. Zhan, Y. F. Lu, and S. F. Chen, *Yangla Copper Deposits of Western Yunnan Province*, China University of Geosciences Press, Wuhan, China, 1998.

[3] L. Q. He, M. G. Zhan, and Y. F. Lu, "Division of sequence stratigraphy and study on ore-bearing beds in Yangla copper ore field, western Yunnan," *Geology and Mineral Resources of South China*, vol. 3, pp. 37–41, 1998.

[4] J. Zhu, P. S. Zeng, L. C. Zeng, and J. Yin, "Stratigraphic subdivision of the Yangla copper ore districtu, northwestern Yunnan," *Acta Geologica Sinica*, vol. 83, no. 10, pp. 1415–1420, 2009.

[5] J. M. Gan, M. G. Zhan, F. M. Yu, L. Q. He, S. F. Chen, and F. L. Dong, "Structural deformation and its ore-control significance in Yangla copper district, Deqing, western Yunnan," *Geology and Mineral Resources of South China*, vol. 14, no. 4, pp. 59–65, 1998.

[6] B. Li, G. F. Zou, S. M. Wen et al., "Fault structure, ore-controlling structural model and prospecting prediction of Yangla copper deposit, northwestern Yunnan," *Mineral Exploration*, vol. 5, no. 5, pp. 699–711, 2014.

[7] S. L. Lin and L. Q. Wang, "Structural features of the Yagra copper deposit in Deqen, Yunnan," *Sedimentary Geology and Tethyan Geology*, vol. 24, no. 3, pp. 48–51, 2004.

[8] P. S. Zeng, G. H. Yin, and W. C. Li, *Tectonic-Magmatic-Metallogenic System of Deqin-Yangla Ore Concentration Area within the Jingshajiang Orogeny*, Geological Publishing House, Beijing, China, 2015.

[9] X. A. Yang, J. J. Liu, S. Y. Han et al., "Mineral composition, geochemistry of the Yangla copper deposit in Yunnan and their geological significances," *Geoscience*, vol. 26, no. 2, pp. 229–242, 2012.

[10] X. Yang, J. J. Liu, D. G. Zhai et al., "Geochemistry of the Yangla volcanic rocks and its relationship to Cu mineralization in the Yangla copper deposit, western Yunnan, China," *Journal of Volcanology and Geothermal Research*, vol. 243-244, pp. 38–44, 2012.

[11] X. A. Yang, J. J. Liu, Y. Cao et al., "Geochemistry and S, Pb isotope of the Yangla copper deposit, western Yunnan, China: implication for ore genesis," *Lithos*, vol. 144-145, no. 7, pp. 231–240, 2012.

[12] X.'a. Yang, J. Liu, S. Han, H. Wang, and S. Chen, "S and Pb isotopic constraints on the relationship between the Linong granodiorite and the Yangla copper deposit, Yunnan, China," *Acta Geologica Sinica - English Edition*, vol. 86, no. 6, pp. 1488–1499, 2012.

[13] L. J. Du, Z. L. Huan, B. Li et al., "Tectono-geochemical features and orientation prognosis of concealed ores of Yangla Cu deposit, Yunnan Province, SW China," *Acta Mineralogica Sinica*, vol. 37, no. 4, pp. 401–409, 2017.

[14] L.-J. Du, B. Li, Z.-L. Huang, J.-X. Zhou, G.-F. Zou, and Z.-F. Yan, "Carbon-oxygen isotopic geochemistry of the Yangla Cu skarn deposit, SW China: implications for the source and evolution of hydrothermal fluids," *Ore Geology Reviews*, vol. 88, pp. 809–821, 2017.

[15] Y. B. Wang, J. Han, P. S. Zeng et al., "U–Pb dating and Hf isotopic characteristics of zircons from granodiorite in Yangla copper deposit, Deqin County, Yunnan, Southwest China," *Acta Petrologica Sinica*, vol. 26, no. 6, pp. 1833–1844, 2010.

[16] X. A. Yang, J. J. Liu, and S. Y. Han, "U-Pb dating of zircon from the Linong granodiorite, Re-Os dating of molybdenite from the ore body and their geological significances in the Yangla copper deposit, Yunnan," *Acta Petrologica Sinica*, vol. 27, no. 9, pp. 2567–2576, 2011.

[17] X. A. Yang, *Superimposed Mineralization and Prospecting Patterns of the Yangla Mineralization Zone in Western Yunnan Province*, China University of Geosciences, Beijing, China, 2012.

[18] X. Y. Meng, *The Petrogenesis of the Skarn and the Magmatic Origin in the Yangla Copper Deposit Area along Jinshajiang Belt, Western Yunnan Province*, China University of Geosciences, Beijing, China, 2016.

[19] J. J. Zhu, *The Geological Setting and Metallogenesis of the Yangla Copper Deposit, SW Yunnan*, Institure of Geochemistry, Chinese Academy of Sciences, Guiyang, China, 2012.

[20] J. Q. Wei, M. G. Zhan, Y. F. Lu, K. X. Chen, and L. Q. He, "Geochemistry of granitoids in Yangla ore district, western Yunnan," *Geology and Mineral Resources of South China*, no. 4, pp. 50–56, 1997.

[21] Y. F. Lu, M. G. Zhan, and K. X. Chen, "U-Pb isotopic dating of basalt from the Gajinxueshan Group in the Jinshajiang tectonic belt," *Regional Geology of China*, vol. 19, no. 2, pp. 155–158, 2000.

[22] R. Gao, L. Xiao, Q. He, J. Yuan, P. Z. Ni, and J. X. Du. Geochronology, "Geochemistry and petrogenesis of granites in Weixi-Deqin, west Yunnan," *Earth Science-Journal of China University of Geosciences*, vol. 35, no. 2, pp. 186–200, 2010.

[23] W. C. Li, G. T. Pan, and Z. Q. Hou, *Metallogenic theory and exploration technique of "Sanjiang" multi-island arc basin-collisional orogeny in southwest China*, Geological Publishing House, Beijing, China, 2010.

[24] L. J. Du, *Hydrothermal Fluid Evolution and the Ore-Forming Mechanism in the Yangla Cu Deposit, Northwestern Yunnan*, Institure of Geochemistry, Chinese Academy of Sciences, Guiyang, China, 2017.

[25] S. Y. Chen, X. X. Gu, W. B. Cheng, G. Zheng, S. Y. Han, and Y. W. Peng, "Characteristics of ore-forming fluid and mineralization process of the Yangla copper deposit, Yunnan," *Earth Science Frontiers*, vol. 20, no. 1, pp. 82–91, 2013.

[26] X. A. Yang, J. J. Liu, L. B. Yang, S. Y. Han, X. M. Sun, and H. Wang, "Fluid inclusion and isotope geochemistry of the Yangla copper deposit, Yunnan, China," *Mineralogy and Petrology*, vol. 108, no. 2, pp. 303–315, 2014.

[27] S. Y. Chen, X. X. Gu, W. B. Cheng et al., "Characteristics of stable isotopic compositions and its geological significances of the Yangla copper deposit, northwestern Yunnan Province," *Acta Petrologica Sinica*, vol. 29, no. 4, pp. 1290–1300, 2013.

[28] S. Y. Chen, *Geological, Geochemical Characteristics and Genesis of the Yangla Copper Deposit, Northwestern Yunnan*, China University of Geosciences, Beijing, China, 2013.

[29] Z. Yang, L. Yang, J. Liu, G. Zhang, F. Long, and Y. Liu, "The discussion on the ore genesis of Yangla copper Deposite, Yunnan, China," *Acta Geologica Sinica - English Edition*, vol. 88, no. s2, pp. 1712-1713, 2014.

[30] J. N. Zhao, *Geological and Geochemical Characteristics of Orebody and Deep Ore Exploration for Yangla Ore Deposit, Western Yunnan*, China University of Geosciences, Beijing, China, 2012.

[31] J. Y. Pan, Q. Zhang, D. S. Ma, and C. Y. Li, "Stable isotope geochemical characteristics of the Yangla copper deposit in western Yunnan Province," *Acta Mineralogica Sinica*, vol. 20, no. 4, pp. 385–389, 2000.

[32] J. Zhu, *Geological, Geochemical Characteristics and Genesis of the Yangla Copper Deposit, Deqin Country, Yunnan*, Kunming University of Science and Technology, Kunming, China, 2011.

[33] J. J. Zhu, R. Z. Hu, X. W. Bi, H. Zhong, and X. Zhang, "Geology, geochemistry, geochronology and genesis of the Yangla skarn copper deposit, Yunnan Province, China," *Acta Geologica Sinica - English Edition*, vol. 87, no. z1, pp. 851-852, 2013.

[34] J. J. Zhu, R. Z. Hu, X. W. Bi, H. Zhong, and H. Chen, "Zircon U–Pb ages, Hf–O isotopes and whole-rock Sr–Nd–Pb isotopic geochemistry of granitoids in the Jinshajiang suture zone, SW China: Constraints on petrogenesis and tectonic evolution of the Paleo-Tethys Ocean," *Lithos*, vol. 126, no. 3-4, pp. 248–264, 2011.

[35] K. X. Chen, J. Q. Wei, and D. P. Yan, "A preliminary study of porphyry bodies and related mineralization in Yangla area, Deqing, western Yunnan," *Geology and Mineral Resources of South China*, vol. 2, pp. 1–8, 1999.

[36] G. Yin and J. Yin, "The superimposed mineralization Andexploration of integrated technology of Yangla copper deposit, northwestern Yunnan," *Acta Geologica Sinica - English Edition*, vol. 88, no. s2, pp. 637-638, 2014.

[37] R. N. Clayton and T. K. Mayeda, "The use of bromine pentafluoride in the extraction of oxygen from oxides and silicates for isotopic analysis," *Geochimica et Cosmochimica Acta*, vol. 27, no. 1, pp. 43–52, 1963.

[38] M. L. Coleman, T. J. Shepherd, J. J. Durham, J. E. Rouse, and G. R. Moore, "Reduction of water with zinc for hydrogen isotope analysis," *Analytical Chemistry*, vol. 54, no. 6, pp. 993–995, 1982.

[39] X. X. He, X. K. Zhu, C. Yang, Q. Feng, and Y. Song, "High-precision analysis of Pb isotope ratios using MC-ICP-MS," *Acta Geoscientica Sinica*, vol. 26, pp. 19–22, 2005.

[40] H. Z. Lu, H. R. Fan, and P. Ni, *Fluid Inclusions*, Science Publishing, Beijing, China, 2004.

[41] T. Driesner and C. A. Heinrich, "The system H_2O-NaCl. Part I: Correlation formulae for phase relations in temperature-pressure-composition space from 0 to 1000 ˚C, 0 to 5000 bar, and 0 to 1 X_{NaCl}," *Geochimica et Cosmochimica Acta*, vol. 71, no. 20, pp. 4880–4901, 2007.

[42] Q. H. Shu, Y. Lai, L. M. Wei, Y. Sun, and C. Wang, "Fluid inclusion study of the Baiyinnuo'er Zn-Pb deposit , south segment of the Great Xing'an Mountain, northeastern China," *Acta Petrologica Sinica*, vol. 27, no. 5, pp. 1467–1482, 2011.

[43] C. Huang, X. H. Li, L. F. Wang, and F. P. Liu, "Fluid inclusion study of the Huangshaping polymetallic deposit, Hunan Province, South China," *Acta Petrologica Sinica*, vol. 29, no. 12, pp. 4232–4244, 2013.

[44] Y. F. Lu, K. X. Chen, and H. L. Huang, "Study on fluid inclusions in different types of copper deposits in Yunnan," *Geological Science and Technology Information*, vol. 23, no. 2, pp. 13–20, 2004.

[45] B. Liu and G. X. Duan, "The density and isochoric formulae for NaCl-H_2O fluid inclusions (salinity≤5wt%) and their applications," *Acta Mineralogica Sinica*, vol. 7, no. 4, pp. 59–66, 1987.

[46] B. Liu, "Density and isochoric formulae for NaCl-H$_2$O inclusions with medium and high salinity and their applications," *Geological Review*, vol. 47, no. 6, pp. 617–622, 2001.

[47] B. Liu, "Calculation of pH and Eh for aqueous inclusions as simple system," *Acta Petrologica Sinica*, vol. 27, no. 5, pp. 1533–1542, 2011.

[48] Y. Matsuhisa, J. R. Goldsmith, and R. N. Clayton, "Oxygen isotopic fractionation in the system quartz-albite-anorthite-water," *Geochimica et Cosmochimica Acta*, vol. 43, no. 7, pp. 1131–1140, 1979.

[49] J. J. Zhu, R. Z. Hu, X. W. Bi et al., "Genesis and tectonic significance of granites in the Yangla ore district, northwestern Yunnan Province," *Acta Petrologica Sinica*, vol. 27, no. 9, pp. 2553–2566, 2011.

[50] Y. F. Zheng and J. F. Chen, *Stable Isotope Geochemistry*, Science Press, Beijing, China, 2000.

[51] H. Ohmoto, "Systematics of sulfur and carbon isotopes in hydrothermal ore deposits," *Economic Geology*, vol. 67, no. 5, pp. 551–578, 1972.

[52] H. Ohmoto and R. O. Rye, "Isotopes of sulfur and carbon," in *Geochemistry of Hydrothermal Ore Deposits*, H. L. Barnes, Ed., pp. 509–567, John Wiley, New York, NY, USA, 2nd edition, 1979.

[53] D. M. Pinckney and T. A. Rafter, "Fractionation of sulfur isotopes during ore deposition in the upper Mississippi Valley zinc-lead district," *Economic Geology*, vol. 67, no. 3, pp. 315–328, 1972.

[54] R. E. Zartman and B. R. Doe, "Plumbotectonics—the model," *Tectonophysics*, vol. 75, no. 1-2, pp. 135–162, 1981.

[55] B. Q. Zhu, *The Theory and Application of the Isotopic Systematic in Geoscience Concurrent Discussion of the Continental Crust and Mantle Evolvement in China*, Science Press, Beijing, China, 1998.

[56] Y. F. Lu, M. G. Zhan, K. X. Chen, and H. Huilan, "Fluid inclusions in ore-bearing skarns from the Yangla copper mineralization concentrated area of Deqin county, Yunnan Province," *Mineral Deposits*, vol. 17, no. 4, pp. 331–341, 1998.

[57] D. H. Zhang, "Overview of research on the ore depositional mechanisms in ore-forming fluid," *Geological Science and Technology Information*, vol. 16, no. 3, pp. 53–58, 1997.

[58] J. T. Liu, *Late-Trassic Cu Mineralization in Porphyry Environment, Northwest Yunnan, China*, China University of Geosciences, Beijing, China, 2014.

[59] Q. L. Feng, M. C. Ge, and D. F. Xie, "Stratigraphic sequence and tectonic evolution in passive continental margin Jinshajiang belt, northwestern Yunnan Province, China," *Earth Science*, vol. 24, no. 6, pp. 553–557, 1999.

[60] L. Q. Wang, G. T. Pan, D. M. Li, X. Qiang, and L. Shiliang, "The spatio-temporal framework and geological evolution of the Jinshajiang arc-basin systems," *Acta Geolcgica Sinica*, vol. 73, no. 3, pp. 206–218, 1999.

[61] L. Q. Wang, G. T. Pan, and D. M. Li, "The evolution and mineralization of the Jomda-Weixi continental marginal volcanic arc, southwestern China," *Sedimentary Geology and Tethyan Geology*, vol. 20, no. 2, pp. 1–17, 2000.

[62] L. Q. Wang, D. M. Li, and S. P. Guan, "The evolution of the Luchun-Hon gponiuchang superimposed rifting basin, Deqin county, Yunnan Province," *Journal of Mineralogy and Petrology*, vol. 21, no. 3, pp. 81–89, 2001.

[63] L. Q. Wang, Z. Q. Hou, X. X. Mo, M. Wang, and Q. Xu, "The post-collisional crustal extension setting: an important mineralizing environment of volcanic massive sulfide deposits in Jinsha orogenic belt," *Acta Geolcgica Sinica*, vol. 76, no. 4, pp. 541–556, 2002.

[64] X. Meng, J. Mao, C. Zhang, D. Zhang, Z. Kong, and F. Jia, "The timing, origin and T-f$_{O2}$ crystallization conditions of long-lived magmatism at the Yangla copper deposit, Sanjiang Tethyan orogenic belt: Implications for post-collisional magmatic-hydrothermal ore formation," *Gondwana Research*, vol. 40, pp. 211–229, 2016.

[65] X. Wang, I. Metcalfe, P. Jian, L. He, and C. Wang, "The Jinshajiang–Ailaoshan suture zone, China: tectonostratigraphy, age and evolution," *Journal of Asian Earth Sciences*, vol. 18, no. 6, pp. 675–690, 2000.

[66] P. S. Zeng, Y. B. Wang, Q. Ma, Z. Q. Wang, and L. G. Wen, "Diachronous collision-closure of the Jinshajiang paleo-ocean basin in the Yangla area: constraints from ages of the granites," *Earth Science Frontiers*, vol. 25, no. 6, pp. 092–105, 2018.

[67] Z. Chen, J. Chen, S. Tian, and B. Xu, "Application of fractal content-gradient method for delineating geochemical anomalies associated with copper occurrences in the Yangla ore field, China," *Geoscience Frontiers*, vol. 8, no. 1, pp. 189–197, 2017.

[68] B. Li, Z. L. Huang, J. X. Zhou, G. Tang, and Y. Liu, "Diagenesis-mineralization and ore prospecting of the Yangla copper deposit, Yunnan Province, southwest China," *Acta Geologica Sinica - English Edition*, vol. 89, no. 5, pp. 1766–1766, 2015.

[69] J. Q. Wei, K. X. Chen, and F. Y. Wei, "Tectonism-magmatism-mineralization in Yangla region, western Yunnan," *Geology and Mineral Resources of South China*, vol. 16, no. 1, pp. 59–62, 2000.